Variations in Seismic Wave Speed and V P / V S Ratio in the North American Lithosphere

Variations in Seismic Wavespeed and Vp/Vs Ratio in the North American Lithosphere

Eva M. Golos[1,2], Hongjian Fang[1], Robert D. van der Hilst[1]

[1]Department of Earth, Atmospheric and Planetary Sciences, Massachusetts Institute of Technology, Cambridge, MA, USA
[2]Now at Department of Earth, Environmental and Planetary Sciences, Brown University, Providence, RI, USA

Key Points:

- We introduce an inversion for V_P, V_S, and V_P/V_S variations at lithospheric scales
- V_P/V_S variations contain novel, geologically significant, information
- Strong V_P/V_S variations may indicate regions of partial melt within or at the base of the lithosphere

This is the author manuscript accepted for publication and has undergone full peer review but has not been through the copyediting, typesetting, pagination and proofreading process, which may lead to differences between this version and the Version of Record. Please cite this article as doi: 10.1029/2020JB020574

Corresponding author: Eva M. Golos, eva_golos@brown.edu

Abstract

Seismic wavespeed is controlled by a number of factors, including temperature and chemical composition, as well as the presence of volatiles and partial melt. Tomography provides a powerful constraint on wavespeed variations, but if only V_P or V_S variations are imaged it is challenging to separate the competing effects of these factors and make a full interpretation of seismic anomalies. In this study, we generate models of variations in the V_P/V_S ratio, which introduce new constraints on geologic structures, compositions, and processes. We invert P and S wave arrival times, as well as Rayleigh wave phase velocities, utilizing the sensitivity of Rayleigh waves to both V_P and V_S to form mutually-constrained but independent models of V_P and V_S structure at lithospheric depths below the continental United States and Southeastern Canada. From this we can examine variations in V_P/V_S, highlighting a distinct pattern of anomalies which are less readily observed in V_P or V_S alone. A clustering analysis is performed to relate 1D profiles of wavespeed as a function of depth to tectonic provinces. While the first-order structure of V_P and V_S appears to be dominated by the thermal contrast between the Eastern and Western US, the strongest control over V_P/V_S ratio perturbations within the mantle lithosphere appears to be the presence of melt. Certain higher-V_P/V_S anomalies within the cratonic interior may reflect compositional anomalies and variations in Moho structure. This work provides a continental-scale framework for future quantitative analyses of thermal and compositional heterogeneity, and for targeted geologic interpretation.

Plain Language Summary

We present a model of 3D wavespeed variations down to 100 km depth below the continental United States and Southeastern Canada. Our inversion includes data from body waves and surface waves, and allows us to constrain both compressional (V_P) and shear (V_S) wavespeed variations. The quantity defined by their ratio, V_P/V_S, can provide additional information about the chemical, thermal, or other origins of seismic anomalies within the crust and upper mantle. Patterns of V_P and V_S variations are similar to one another and to previous models, showing fast wave propagation in the Eastern US and slow propagation in the West, likely controlled mainly by temperature. Meanwhile, V_P/V_S seems to be sensitive to other processes in the uppermost 60 km, as the east-west dichotomy is not the dominant visual feature. We suggest that partial melting within or at the base of the lithosphere is responsible for the strongest V_P/V_S ratio perturbations, and thus plays an important role in shaping the seismic signature and the dynamics of the lithosphere. Variations in mineral composition of mantle rocks may be responsible for other features in the stable eastern portion of the continent.

1 Introduction

Seismic tomography below the continental United States shows that P and S wavespeed anomalies are highly correlated in the crust and upper mantle (Burdick et al., 2017; Schmandt et al., 2015; Schmandt & Lin, 2014; Shen & Ritzwoller, 2016; Porritt et al., 2014; Porter et al., 2016; Zhu et al., 2017), and both V_P and V_S have historically been assumed to depend on temperature (Goes & van der Lee, 2002; Priestley & Tilmann, 2009). In contrast, variations in the ratio of V_P to V_S (V_P/V_S), related to Poisson's ratio, are sensitive to a range of thermal, chemical, and anelastic processes (Christensen & Mooney, 1995; Karato & Karki, 2001; Masters et al., 2000; Trampert et al., 2001). Systematic analysis of variations between V_P, V_S, and V_P/V_S may therefore provide insight into the interplay between these processes and how they influence seismic anomalies.

V_P/V_S is less sensitive to temperature than isotropic V_P or V_S alone, but is strongly sensitive to the presence of fluids and melt (Chantel et al., 2016; Hammond & Humphreys, 2000). This is in part due to the melt itself, as porous media have reduced shear wavespeeds, and in fact the geometry and connectivity of individual pockets is important (Hammond & Humphreys, 2000; Takei, 2002). In addition, anelasticity within near-solidus rock strongly increases V_P/V_S (Faul & Jackson, 2005; Takei, 2017). At lithospheric scales, the presence and scale of melt can provide insight into tectonic processes and mantle flow by indicating asthenospheric upwelling, fluid release, and perhaps anatectic melting (Patiño Douce et al., 1990). Furthermore, melt is thought to play an important role in defining the base of the lithosphere, especially in active tectonic settings (Rychert & Shearer, 2009; Tharimena et al., 2017). Therefore, identifying and mapping the distribution of melt facilitates understanding of the factors that govern lithospheric structure, plate tectonic evolution, and lithosphere-asthenosphere interactions, and V_P/V_S may be a crucial tool for doing so.

Mineral-scale processes, for instance the garnet-spinel phase transition or the formation of pyroxene, also uniquely affect V_P/V_S (Afonso et al., 2010; Baptiste & Tommasi, 2014; Lee, 2003), so this ratio may be used to infer the presence of specific mineral phases. Phase stability is dependent on pressure and temperature, but may also evince chemical alteration and thus yield insight into the geologic history of the mantle. Apart from the aforementioned anelastic effects of partial melt, as melt is removed from the host rock components such as iron, aluminum, and volatiles are preferentially extracted (Jordan, 1988; Schutt & Lesher, 2006, 2010, and references therein), and this signature remains after the melt-generating processes have dissipated. In the olivine and pyroxene mineral systems, which dominate ultramafic mantle rocks, the loss of iron endmembers (or relative enrichment of magnesium) is often used as a proxy for tracking the thermochemical evolution of the lithospheric mantle (e.g. Perry et al., 2003). Other relevant chemical changes that affect V_P, V_S, and V_P/V_S include metasomatic enrichment of silica as a result of interaction with fluids, which is often manifested as an increase in orthopyroxene (Boyd, 1989; Kelemen et al., 1998; Wagner et al., 2008). Additionally, the formation of hydrous minerals can lead to velocity reduction and rheologic weakening, and may indicate subduction or other fluid-generating or transporting processes (Humphreys et al., 2003).

As these thermal, melt-related, and geochemical processes may coexist and interact with one another, simultaneous constraints from multiple seismic and geophysical observables help reduce the nonuniqueness of interpretation. Kennett et al. (1998) recognized this in an early global inversion for both shear wavespeed and bulk sound speed. In this study we focus on V_P/V_S as a tool to distinguish the thermal and geochemical fingerprints of various tectonic and geodynamic processes, in order to better understand the assembly and evolution of continents.

Variations in V_P/V_S have been assessed from seismic observations as well as thermodynamic modeling. Studies have estimated V_P/V_S from H-κ stacking for regional (Purevsuren, 2014; Zandt et al., 1995; Zhu & Kanamori, 2000) and continental (Chevrot & van der Hilst, 2000; Ma & Lowry, 2017; Ramesh et al., 2002) regions of study, but this method has high uncertainty in V_P/V_S. Furthermore, H-κ stacking cannot account for complicated or dipping Moho structures (Zhang et al., 2016), and it is not designed for investigating the lithospheric mantle.

Quantifying 3D variations of V_P/V_S throughout the continental lithosphere is important for interpreting V_P and/or V_S maps to answer questions related to larger-scale features in the Earth, but this property has not been evaluated extensively at whole-lithospheric scales. Fang et al. (2016, 2019) develop tomographic models of V_P/V_S at a smaller scale within Southern California, but they rely on local earthquake data and their technique cannot yet be transferred to continental scales due to computational restrictions. Studies that do report V_P/V_S over larger areas (Hejrani et al., 2015; Schmandt & Humphreys, 2010; Tesoniero et al., 2015; Wei et al., 2018) derive these estimates from separate models of V_P and V_S, which may introduce bias from different ray coverage, smoothing, and other regularization strategies that have been applied (Kennett et al., 1998).

In this paper we introduce a model of variations in V_P and V_S beneath the continental United States using a ray-based joint inversion of body wave and surface wave travel-time data. Incorporating data from multiple seismic phases improves resolution because they are sensitive to the Earth's structure in complementary ways (Golos et al., 2018; Obrebski et al., 2011; Rawlinson & Fishwick, 2012). We estimate variations in V_P/V_S from these two quantities; as V_P and V_S are independent parameters of the same model, we avoid the aforementioned problems associated with estimating V_P/V_S from separate inversions. As we will discuss, weighing different data sets present challenges, but obtaining two independent and mutually constrained parameters enables a more robust interpretation than can be done from just V_P or V_S alone. Adjoint tomography is another way to incorporate information from multiple frequencies to constrain multiple geophysical parameters (Fichtner et al., 2009; Zhu et al., 2017), but the computational burden of such methods poses a disadvantage. We refer to Golos et al. (2018) for a justification of the use of a linearized travel-time framework.

We perform a global inversion, though interpretation is restricted to the continental United States where data coverage is relatively dense and uniform. The resulting model is largely consistent with prior models of V_P and V_S, but variations in V_P/V_S provide novel information that sheds light on several geologic processes. Furthermore, we perform a clustering exercise to demonstrate that all three parameters show spatial variations that are consistent with known tectonic provinces, and that their geologic history governs seismic properties even at depth within the lithosphere. The contrast between the eastern and western portions of the continent, which is largely a thermal difference, is sufficient to explain the first-order structures, but in other regions different processes must be invoked. In particular, we highlight several regions where partial melt could be responsible for strong anomalies in V_P/V_S. This method will aid in the quantification of large-scale thermal and chemical heterogeneity within the lithosphere, but such analysis is left to future papers.

2 Methods

The inversion method followed here is an extension of that presented by Golos et al. (2018), who used a linearized explicit joint inversion of surface and body waves to examine deviations in shear wave slowness. Here the inversion is reformulated to include P body wave data and so account for variations in compressional and shear slowness (δS_P and δS_S, respectively). In this study we use ray theory to describe traveltime data and sensitivity kernels, but finite-frequency tomography could also be used.

For body waves, S and P slowness variations are parameterized following ray theory (Aki & Lee, 1976; Spakman & Nolet, 1988), and we compute travel-time deviations from the AK135 reference model (Kennett et al., 1995). For an observation of a P wave phase (e.g., P, Pn, pP), we have

$$\delta t^P = \sum_{k=1}^{K} \delta S_{P,k} \Delta l_k, \tag{1}$$

where δt^P is the travel-time residual, $\delta S_{P,k}$ refers to compressional wave slowness (that is, $\frac{1}{V_P}$) perturbations, and Δl_k signifies summation along the raypath. In matrix form, we have

$$\boldsymbol{\delta t^P} = \boldsymbol{G^P_{V_P} \delta S_P}. \tag{2}$$

Similarly, for S waves:

$$\boldsymbol{\delta t^S} = \boldsymbol{G^S_{V_S} \delta S_S}. \tag{3}$$

For Rayleigh waves, we recall the direct-dispersion linear formulation from Fang et al. (2015); Golos et al. (2018) (adapted to the notation used here):

$$\delta t^{SW}(\omega) = \sum_{k=1}^{K} \frac{\nu_k}{C_k^2(\omega)} \sum_{j=1}^{J} [R_\rho(z_j) \frac{\partial C_k(\omega)}{\partial \rho_k(z_j)} + R_\alpha(z_j) \frac{\partial C_k(\omega)}{\partial V_{P,k}(z_j)} + \frac{\partial C_k(\omega)}{\partial V_{S,k}(z_j)}] V_{S,k}(z_j)^2 \delta S_{S,k}(z_j). \tag{4}$$

The superscript SW indicates surface wave measurements; ν_k is the bilinear interpolation coefficient for entry k; $C_k(\omega)$ is the phase velocity at frequency ω; R_ρ accounts for scaling between density, ρ, and V_S; R_α accounts for scaling between V_P and V_S. We retain δS_P as an independent parameter and include the scaling for density in this S_P term. Now we have:

$$\delta t^{SW}(\omega) = \sum_{k=1}^{K} \frac{\nu_k}{C_k^2(\omega)} \left[\sum_{j=1}^{J} [R_\rho(z_j) \frac{\partial C_k(\omega)}{\partial \rho_k(z_j)} + \frac{\partial C_k(\omega)}{\partial V_{P,k}(z_j)}] V_{P,k}(z_j)^2 \delta S_{P,k}(z_j) + \sum_{j=1}^{J} \frac{\partial C_k(\omega)}{\partial V_{S,k}(z_j)} V_{S,k}(z_j)^2 \delta S_{S,k}(z_j) \right]. \tag{5}$$

In matrix form:

$$\boldsymbol{\delta t^{SW}} = \boldsymbol{G_P^{SW}} \boldsymbol{\delta S_P} + \boldsymbol{G_S^{SW}} \boldsymbol{\delta S_S}. \tag{6}$$

P, S, and surface wave data are inverted simultaneously for $\boldsymbol{\delta S_P}$ and $\boldsymbol{\delta S_S}$ using a LSQR iterative solver.

We minimize the cost function

$$\epsilon = ||\boldsymbol{Gm} - \boldsymbol{d}||^2 + c_1 ||\boldsymbol{Lm}||^2 + c_2 ||\boldsymbol{m}||^2. \tag{7}$$

$\boldsymbol{G}$ is a block matrix containing the P, S, and Rayleigh wave sensitivity expressions, $\boldsymbol{m}$ is the model containing $\boldsymbol{\delta S_S}$ and $\boldsymbol{\delta S_P}$, and $\boldsymbol{d}$ contains all traveltimes. The matrix $\boldsymbol{L}$ is a first-derivative smoothing operator. The constants c_1 (which controls smoothing) and c_2 (which controls damping on the L2-norm) are chosen based on the L-curve method, in which the fit of data and effects of regularization are balanced. As in Li et al. (2008); Burdick et al. (2017); Golos et al. (2018), we perform the inversion on a grid with adaptive spacing, where smaller cells in regions of high ray density allow resolution of smaller-scale features.

From the model of δS_P and δS_S, we use a chain rule expansion to estimate variations in V_P/V_S, assuming the deviations are small (of the order of a few percent):

$$\delta(V_P/V_S) = -\frac{V_P^2}{V_S} \delta S_P + V_P \delta S_S = \frac{1}{V_S} \delta V_P - \frac{V_P}{V_S} \delta V_S. \tag{8}$$

The inversion problem may also be parameterized in terms of V_P and V_P/V_S. The latter approach has been used in local and regional studies (Eberhart-Phillips & Fry, 2017; Fang et al., 2019; Rocker et al., 2006; Thurber et al., 1995) but has not previously been used on continental scales. In the Supporting information we describe this alternate formulation and compare its results and performance on synthetic tests to the inversion described in detail above. For the purposes of this paper we are interested in image reconstruction, and the $V_P + V_S$ formulation resolves features more robustly.

3 Data

3.1 Body Wave Data

The majority of body wave data used are from the USArray Transportable Array, but we also leverage several regional networks. The data are clustered so that rays that are over-represented in the data are averaged and do not bias the inversion.

For P waves, we use >4 million arrivals from USArray and the EHB-ISC bulletin (Engdahl et al., 1998), which are clustered into 1.6 million summary rays. We also incorporate about 12,000 picks from the dataset of Boyce et al. (2016), who combine several regional networks in Southeastern Canada, and about 670 P arrivals from the Archean-Proterozoic Transect (APT) experiment (Silver et al., 1993). These regional picks were originally made as relative travel-times and the Absolute Arrival-Time Recovery Method (AARM) was used to convert to absolute travel time residuals with respect to AK135 (Boyce et al., 2017). Incorporation of data from Southern Canada improves resolution near the Great Lakes and reduces artifacts at the northern edge of the USArray network. Finally, we include 145,000 clustered Pn arrivals from the EHB-ISC bulletin, which provide additional sensitivity at the top of the lithospheric mantle. Figure 1a-b show source and receiver distributions for P and Pn data, respectively.

Figure 1. Source-receiver distribution for the body wave data set: Locations of seismograph stations (blue) and epicenters of earthquakes (red) from the USArray and EHB data used in our inversions. (a) Direct P arrivals; (b) Pn phase arrivals; (c) Direct S arrivals.

The S wave dataset includes about 600,000 direct S arrival times from the TA network, the EHB-ISC Bulletin, and the Canadian networks; after clustering, there are about 370,000 unique summary rays. The station and event locations for S waves are depicted in Figure 1c.

All body wave arrival times are corrected for the travel-time anomalies due to Earth ellipticity and station elevation, as in Burdick et al. (2008). In addition, we provide a correction to account for the difference in Moho depth between the AK135 model and a more accurate Moho depth model (Schmandt et al. (2015) within the U.S., Szwillus et al. (2019) outside of the U.S.).

We do not correct for radial or azimuthal anisotropy, nor for attenuation. The effects of these were shown to be small in a linear, ray theoretical inversion scheme by Golos et al. (2018). We refer readers to the discussion in that study.

3.2 Surface Wave Data

We calculate travel-time anomalies from phase velocities of Rayleigh waves from several sources. We utilize 160,000 measurements from the USANT dataset of Ekström (2017), which are taken from ambient noise cross-correlations between USArray stations at periods of 5-40 s. The stations used in these measurements are shown in Figure 2a. At longer periods, we use 140,000 data from Schaeffer and Lebedev (2014), which are derived from earthquake recordings, and span periods of 45 - 290 s (Figure 2b).

Additionally, to improve resolution below the Great Lakes and in Southern Canada we use about 22,000 phase velocities from periods of 10-290 s from Petrescu et al. (2017), and about 76,000 phase velocities at 8-210 s from the dataset of Foster et al. (2020). Both studies used the two-station method to obtain path-averaged phase velocity measurements between stations, the locations of which are shown in Figure 2c.

Figure 2. Surface wave data used in $V_P + V_S$ inversion. (a) Stations used in cross-correlation from USANT15 database (Ekström, 2017). (b) Event (red) and receiver (blue) locations used from SL2013NA database (Schaeffer & Lebedev, 2014). (c) Northern US/Southern Canada stations used by Petrescu et al. (2017) and Foster et al. (2020).

Figure 3. Depth-varying sensitivity of Rayleigh waves to V_P and V_S. (a) Periods of 10 - 100s. Sensitivity was determined using *surfdisp96* (Herrmann, 2013). (b) Periods > 100s. Sensitivity was calculated using the *Mineos* package.

For phase velocity measurements at periods <100 s, we use *surfdisp96* (Herrmann, 2013) to calculate the 1D sensitivity-depth relationship. We use a modified AK135 reference model, which has vertical cell spacing of ∼11 km and monotonically-increasing wavespeeds with depth in the crust. For periods >100 s, we use the *Mineos* code of Masters et al. (https://geodynamics.org/cig/software/mineos/) to generate sensitivity kernels. Figure 3 shows the depth-sensitivity relationship for V_P and V_S for a selection of periods represented in our data. We note that V_P sensitivity begins to diminish below about 60 km, even for the longest-period measurements in our dataset. The Pn data somewhat combat this effect.

4 Results

4.1 Uncertainty and Resolution

4.1.1 Model Uncertainty and Data Fit

Quantifying error in travel-time tomography models is difficult as the true model is not known. What can be examined is relative uncertainty introduced by the inversion as well as the variance reduction of the data misfit. As other published models are derived using different inversion schemes, and do not usually report model uncertainty, there is no metric we can easily rely on to evince improvements offered by our method. Indeed, no other model known to the authors estimates 3D variations of V_P/V_S for the entire United States at the resolution offered by the TA.

A bootstrapping analysis was performed to estimate uncertainty in the δV_P and δV_S models of MITPS_20. 50 inversions were performed using 90% of the full dataset; furthermore, the errors in data fit were randomly resampled in order to add noise to the bootstrapping inversions. The standard deviation of the resulting models may be used as a proxy for uncertainty from the inversion. Mean uncertainty is around 0.1% for δV_P (rarely exceeding 0.4%), and 0.2% for δV_S (rarely exceeding 0.5%). As these anomalies are roughly a tenth of the magnitude of anomalies in MITPS_20, we conclude that stability and precision of our inversion are satisfactory. Maps displaying the geographic distribution of uncertainty may be found in the Supporting Information.

-	Variance Reduction	std($\boldsymbol{\delta t}$)	std($\boldsymbol{\delta t} - \mathbf{Gm}$)
Rayleigh Waves	93.7%	9.6 s	2.4 s
S waves	54.3%	5.0 s	3.4 s
P waves	27.2%	2.1 s	1.8 s
All data	81.0%	5.4 s	2.3 s

Table 1. Variance reduction for different data sets in model MITPS_20. Left column: variance reduction. Center column: standard deviation of all travel-time perturbations (the input data for inversion). Right column: standard deviation of data residuals, i.e. observed - modeled traveltime perturbations.

Figure 4. Checkerboard test results for V_P+V_S inversion. Top: 5-by-5° synthetic model of V_P, V_S, and V_P/V_S variations. Bottom: inversion results for V_P, V_S, and V_P/V_S models at depths of 20, 60, and 100 km.

Figure 5. Checkerboard test results for V_P+V_S inversion. Top: 1.5-by-1.5° synthetic model of V_P, V_S, and V_P/V_S variations. Bottom: inversion results for V_P, V_S, and V_P/V_S models at depths of 20, 60, and 100 km.

To quantify how well we fit different data, we calculate the variance reduction (VR) for our overall dataset, as well as for surface waves, P waves, and S waves. Table 1 reports these values, as well as standard deviations of the input data and data residuals ($\boldsymbol{\delta t}-\boldsymbol{G\hat{m}}$). The values of VR for surface wave and S wave data are comparable to those obtained in the V_S-only model of Golos et al. (2018), so including V_P as a parameter does not appreciably change the overall fit of those data. VR is lower for the P-wave data (P and Pn phases), but this is because the magnitudes of travel-time anomalies are low, so the data residuals, although also small, do not decrease dramatically. Tesoniero et al. (2015) also find that VR of P wave arrival data is about half of that of S waves. A test which included a correction for radial anisotropy within the S-wave data did not appreciably change any of the variance reductions.

4.1.2 Checkerboard Tests

We perform checkerboard resolution tests for 5°-x-5° and 1.5°-x-1.5° and checkerboard patterns. The synthetic models and corresponding inversion results are shown in Figures 4 and Figure 5. The diagnostic value of such a test is limited (van der Hilst et al., 1993; Lévěque et al., 1993), but it does provide a qualitative sense of horizontal resolution, particularly where the shapes and amplitudes of input anomalies are not recovered accurately.

δV_S is recovered adequately and uniformly across the US and Southeastern Canada for both the 5° and 1.5° tests. Amplitudes diminish below 60 km depth, but lateral resolution of features remains good. δV_P is not recovered as consistently at 60 km; because Pn waves tend to come from sources in the southwest, the model below the Western US preserves amplitudes better than the Eastern part of the country. Despite this discrepancy, the geometry and amplitudes of the V_P/V_S anomalies are recovered adequately at 20 and 60 km, and the geometry is still preserved at 100 km depth.

The major challenge with the V_P+V_S inversion is that the maximum sensitivity of Rayleigh waves to V_P occurs at shallower depths compared to V_S for a given frequency (Figure 3). This discrepancy is exacerbated at longer periods. For the modes and frequencies used in our surface wave data, amplitudes of features in the δV_P model cannot be recovered adequately below about 100 km depth. Therefore, while we may still interpret features in the δV_S portion of the model below 100 km, we do not examine δV_P or $\delta(V_P/V_S)$ variations at these depths.

Recovery improves at depths where body wave raypaths cross one another, about 300 km, in agreement with Golos et al. (2018). This is, however, deeper than most of the continental lithosphere we are interested in imaging.

4.2 Model description

Figure 6. Horizontal slices through δV_P model. Geologic regions outlined in black are: Superior Province (SP), Appalachian Mountains (A), Mississippi Embayment (ME), Colorado Plateau (CP), Wyoming Province (WY), Basin and Range (BNR), Columbia Plateau (Col) from the USGS Physiographic Provinces database (*https://water.usgs.gov/GIS/metadata/usgswrd/XML/physio.xml*). Red curve shows the Grenville Front (GF) (Whitmeyer & Karlstrom, 2007).

Figure 7. Horizontal slices through δV_S model. Regions outlined are the same as Figure 6.

Figure 8. Horizontal slices through $\delta(V_P/V_S)$ model. Regions outlined are the same as Figure 6.

To a first order, the V_P and V_S anomalies observed in our model agree with other published models, and they resemble one another. Figures 6, 7, and 8 depict horizontal slices through the preferred model, MITPS_20, for δV_P, δV_S, and $\delta(V_P/V_S)$, respectively. Depths range from 20-200 km. Southeastern Canada broadly resembles the Northeastern and North-Central US in structure, with high δV_P and δV_S, and low $\delta(V_P/V_S)$. We do not include stations from Western Canada, therefore that portion of our model takes on the background value in each slice.

The Western US is characterized by low wavespeeds in the upper ∼200 km, whereas high wavespeeds dominate the the Central and Eastern US. Thermal effects are likely the primary control on this pattern, as the seismic anomalies show agreement with features in surface heat flow data (Blackwell et al., 2011), as well as temperature estimates of the upper mantle inferred from thermochemical modeling (Kaban et al., 2014; Khan et al., 2011; Perry et al., 2003) and from Pn tomography (Schutt et al., 2018).

In the Eastern US, $\delta(V_P/V_S)$ is mostly negative at lithospheric depths but is punctuated by higher values, particularly within the 40 and 60 km depth slices. These higher $\delta(V_P/V_S)$ regions are correlated with moderate-amplitude negative V_P and V_S anomalies, and generally trend northeast-to-southwest, consistent with the strike of the major Proterozoic tectonic boundaries (Whitmeyer & Karlstrom, 2007). Synthetic inversions indicate that these features are well resolved (see Section 4.1.2). This suggests a compositional origin for these anomalies, as Proterozoic features are unlikely to impart a thermal anomaly. Several of these features correspond to localities where thick or anomalous crust has been identified: these include the southern Wyoming Province, where crustal thickness may exceed 50 km depth (Shen & Ritzwoller, 2016); the Midcontinent Rift, which has a deep Moho due to sub-crustal underplating (Stein et al., 2018; Zhang et al., 2016); and the Illinois Basin/Reelfoot Rift area (Southern Illinois and Missouri), which exhibits a sharp increase in depth to Moho (Yang et al., 2017). In these regions of underplating or deep Moho, at 40-60 km depth our seismic data sense crustal or basaltic rocks, which have lower wavespeed and higher V_P/V_S than typical mantle compositions (e.g. Shillington et al., 2013).

The Gulf Coast and Mississippi Embayment region have positive $\delta(V_P/V_S)$, and negative δV_P and δV_S within the crust. No strong anomalies are observed from 40-60 km, but below that V_P/V_S is again elevated and wavespeed is low. The low wavespeeds at depth >60 km may occur because our data are sensitive to the asthenosphere below a thin lithosphere: the signature resembles that of the Western US, and furthermore Krauss and Menke (2020) suggest that there may be asthenospheric upwelling below the Gulf Coast. As in the Western US, additional mechanisms beyond a thermal contrast between the lithosphere and asthenosphere are needed to explain the V_P/V_S anomaly. The crustal anomaly may be due partially to sedimentation, but more work must be done to determine the origin of this anomaly.

Some differences are identified between our model and other studies. Firstly, the incorporation of data from surface waves allows us to image features at shallower depths than what is typically resolvable from body-wave tomography. Anomalies in the crust are distinct from the lithospheric mantle (for instance, δV_S decreases and $\delta(V_P/V_S)$ increases substantially from 20 km to 80 km below central Colorado). Furthermore, the amplitudes of variation in the upper 100 km are greater than those derived from body waves only (e.g. Bedle & van der Lee, 2009; Burdick et al., 2017; Schmandt & Lin, 2014).

4.3 Qualitative comparison of V_P/V_S with other published models

Figure 9. Comparison of our $\delta V_P/V_S$ model to Ma and Lowry (2017). Slices of $\delta(V_P/V_S)$ from MITPS_20 at crustal and near-crustal depths, and map of bulk crustal V_P/V_S reported by Ma and Lowry (2017).

We compare the 20-km depth slice of our 3D $\delta(V_P/V_S)$ variations to the bulk crustal V_P/V_S values found via H-κ stacking by Ma and Lowry (2017) in Figure 9. Although (Ma & Lowry, 2017) report uncertainty of 0.07 in V_P/V_S, which is larger than the magnitude of anomalies in MITPS_20, both models image similar structures at crustal depths. Low $\delta(V_P/V_S)$ is identified in the Basin and Range Province, most prominently in southern Arizona. California shows strong small-scale variations, with high values below the Sierra Nevada and low values in the adjacent Central Valley. The Snake River Plain and Yellowstone have higher V_P/V_S than adjacent regions. Some features are misaligned slightly between the two models (e.g. the strong negative anomaly of the Idaho Batholith in (Ma & Lowry, 2017) is further east in MITPS_20), but this may be attributed to the effects of smoothing and/or uneven ray coverage near the edge of the USArray.

Figure 10. Comparison of our $\delta(V_P/V_S)$ model to Tesoniero et al. (2015). $\delta(V_P/V_S)$ variations from MITPS_20 and from SPani Tesoniero et al. (2015) at 100 km depth.

For the mantle structure, we compare our model to SPani (Tesoniero et al., 2015), which also describes V_P and V_S variations obtained from a linear inversion of body and surface wave data. Unlike the inversion described here, Tesoniero et al. (2015) solve for a radially anisotropic model which is then averaged to obtain isotropic δV_P and δV_S. Furthermore, SPani imposes additional constraints on V_P/V_S via regularization. SPani is designed to resolve global-scale structures, so its parameterization is coarser: the authors perform the inversion on a regularly-spaced grid of 5°-x-5° so features will necessarily appear smoothed compared to MITPS_20.

$\delta(V_P/V_S)$ variations from MITPS_20 and SPani at 100 km depth are displayed in Figure 10. The values of SPani are shown as percent variations from the mean V_P/V_S in that slice, so the two models present comparable metrics. As SPani has coarser resolution in the United States, we cannot compare smaller-scale features. Nonetheless, the first-order patterns are similar, with high $\delta(V_P/V_S)$ in the Western US and low V_P/V_S extending from the Great Plains over the Midwest. MITPS_20 has mostly negative $\delta(V_P/V_S)$ in the Eastern US with occasionally positive anomalies, particularly in New England, whereas SPani has a more pronounced positive V_P/V_S excursion over the Eastern states. Also, the magnitude of variation in SPani is stronger and on average higher than in MITPS_20. Some of this discrepancy may reflect the choice of regularization, but large portions of the Western US in SPani have $\delta(V_P/V_S)$ >3%, which is difficult to explain without invoking widespread partial melt. It is surprising that the variations are so large in SPani considering the additional inversion constraints designed to keep V_P/V_S variations near a value derived from mineral physics, and therefore should penalize strong heterogeneity.

5 Discussion

5.1 Cluster Analysis

As a preliminary analysis, we connect 3D variations in our model to features that have been determined by surface and crustal geologic and geophysical studies. We have already noted regions where features in δV_P and $\delta(V_P/V_S)$ correspond to well-known geologic provinces, such as the Rio Grande Rift, the Basin and Range, and the Mississippi Embayment. Here, we investigate whether such provinces extend throughout the lithosphere, and/or where deeper structures may play a role in determining seismic characteristics (and therefore guide tectonic/geodynamic response to forcings or yield insight about lithospheric evolution).

Rather than interpret our model within predefined geological provinces, as Simons et al. (1999) did for Australia, we follow Eymold and Jordan (2019) and determine provinces with similar depth structure according to MITPS_20. We derive 1D profiles of δV_P and $\delta(V_P/V_S)$ with depth and use the k-means++ package in Matlab (version R2020a) to define geographic clusters based on both of these parameters.

Figure 11. Normalized variance for all profiles and all clusters. Results are displayed with number of clusters k ranging from 2 to 10, and for 50 trials.

The number of clusters is a subjective choice. To inform this choice, we calculate the total variance Var_k for all clusters in 50 trials while varying the number of clusters, k, following Eymold and Jordan (2019). k ranges from 2 to 12. We find that the initial seeding of clusters matters more than reported in previous studies, perhaps because our model encompasses a larger region. The results are shown in Figure 11. All values are normalized with respect to Var_1, i.e. the total variance of the model. The optimal number of trials was chosen to be 9, as this number has a smaller spread of Var_k among trials than 7 or 8, but $k >9$ does not substantially improve Var_k.

Figure 12. (a) Points on an interpolated regularly-spaced grid, colored according to the k-means cluster from 50 trials. (b) Probability over 50 trials that k-means will assign a given point to the clusters shown above. (c) Vertical profiles of the cluster-averaged value of δV_S at lithospheric depths. (d) 1D wavespeed-depth profiles of the cluster-averaged value of $\delta(V_P/V_S)$ at lithospheric depths.

Figure 12a displays the geographic cluster most frequently assigned to the points from our model in the trials described above. The separation between the tectonically active WUS and cratonic EUS is immediately apparent. The probability that a given trial places a point within its assigned cluster is shown in Figure 12b. This is a proxy for the stability of the configuration; points on the edges of clusters tend to have lower probability, particularly in regions associated with rapid changes from positive to negative wavespeed anomalies such as the transition from Eastern to Western US.

The center of the Superior Province (SP) has lower (though still ~60%) cluster probability because in 42% of trials this region is assigned to its own unique cluster, rather than the configuration shown here. The cratonic, Archean, SP has a unique seismic, thermal, and perhaps chemical, structure (e.g. Darbyshire et al., 2013; Jaupart et al., 1998, 2014; Pollack, 1986), and the relatively high likelihood of it being an independent cluster reflects its extreme properties. The adjacent areas that are always associated with

Cluster 1 include the southeasternmost Superior Province, but also the Penokean Province (P), which is comprised of Archean-aged bedrock but accreted more recently to the margin of Laurentia (Schulz & Cannon, 2007; van Schmus & Bickford, 1981). Its underlying lithosphere may have different properties than the SP. These differences are not large enough to warrant the creation of a new cluster, but they do emphasize the trade-offs associated with choosing k.

Other regions with (past or present) shared geologic history, such as the Proterozoic parts of the North American shield (Cluster 2) and the Basin and Range (Cluster 9), are identified by the clustering. The boundary between Clusters 2 and 3 is demarcated by the Grenville Front from Kentucky into Canada with high probability. One can conclude that these prominent features have distinct seismic characteristics not just at the surface, but well into the lithosphere.

Figures 12(c,d) depict the vertical structures represented by these clusters for δV_S and $\delta(V_P/V_S)$, respectively. Although δV_S was not explicitly used to form the clusters, the clusters have a meaningful association with changes in δV_S with depth. Additionally, since δV_S has more complete depth-resolution than the other parameters it is the best choice for examining whole-lithospheric properties.

The difference between the high-V_S Eastern US (Clusters 1-5) and low-V_S Western US (clusters 6-9) is persistent throughout the upper 300 km of the Earth. In the WUS, δV_S decreases steeply with depth until about 100 km depth; below this V_S anomalies are fairly steady, and then increase at ∼150-170 km. We interpret the minimum as a low-velocity zone (LVZ) below the lithospheric mantle, and the sharp decrease is inferred to be the LAB. In the Eastern US no LVZ is observed–in fact, δV_S increases slightly in the upper 50 km, and then decreases gradually. This decrease with depth is especially gradual in Clusters 1 and 2, consistent with RF observations of a diffuse and deep LAB in cratonic settings (Abt et al., 2010; Mancinelli et al., 2017).

$\delta V_P/V_S$ (panel d) increases sharply in the WUS from ∼50-80 km depth, then decreases at depths greater than 150 km. The EUS is marked by a decrease in $\delta V_P/V_S$ which is sharpest at crustal depths, and then a gradual increase. The inverse relationship of V_S and V_P/V_S is apparent from this behavior, but clearly does not capture the complexity of the interplay of these variables. For instance, Clusters 1 and 2 both have maxima in δV_S at a similar depth within the crust, but the minimum $\delta V_P/V_S$ occurs around 80 km for Cluster 2, and deeper, around 120 km, in Cluster 1. Both parameters therefore yield useful, independent, information about the lithosphere.

Clusters 7-9, in the West, are controlled by deep structures rather than bedrock geology. Cluster 8 (yellow) tracks near Clusters 7 and 9 in the upper 100 km. However, below this depth, a steep increase in δV_S with depth is apparent in Cluster 8. Likewise, the $\delta(V_P/V_S)$ profile of Cluster 8 resembles its neighbors at shallow depths, but decreases more quickly below 100 km compared to the adjacent Clusters. In map view, Cluster 8 appears just east (downdip) of the Cascade Range, as well as in portions of Southern California; the former corresponds to subducted oceanic lithosphere, while the latter coincides spatially with the Isabella Anomaly. The Isabella anomaly, a high-wavespeed near-vertical feature extending to ∼300 km depth (Bernardino et al., 2019), has been explained by either a fossil remnant of a subducting slab, or alternatively by foundering lithosphere from the Sierra Nevada (Bernardino et al., 2019; Wang et al., 2013). Both subduction zones and lithospheric drips predict cold, possibly eclogitized, lithospheric material in the asthenosphere, which would account for the increase in δV_S with depth. Above such features, fluid released from dehydration reactions may promote melt, which could explain the low δV_S and high $\delta(V_P/V_S)$ around 100 km depth.

Below 80 km depth, Cluster 9 contains the lowest δV_S and the highest $\delta(V_P/V_S)$, but from ∼35-65 km, Cluster 7 (orange) has more extreme values of both parameters.

Figure 13. Vertical cross-sections of δV_S (top left), and $\delta(V_P/V_S)$ (top right) variations across 3 cross sections. The map displays cross-section locations. The grey dashed lines in the profiles indicate depths of 35 km (typical continental Moho) and 100 km (typical lithosphere depth extent). The white lines in sections A-A' and B-B' depict where $\delta(V_P/V_S) \geq 2.0\%$, our inferred threshold for the presence of partial melt following Hammond and Humphreys (2000).

These points are proximal to the Yellowstone Hotspot, Rio Grande Rift, and parts of the Cascades Range—areas where partial melt could be expected due to high heat flow (for the former two), and subduction-related magmatism (the latter). The following Section examines more closely several regions where melt is most likely to be found.

5.2 Inference of melt from V_P/V_S

As alluded to in the Introduction, V_P/V_S is highly sensitive to the presence of fluids and partial melt. Melt plays a crucial but thus far poorly-understood role in continental dynamics, particularly in defining the depth extent of the lithosphere; in understanding asthenospheric and deeper-mantle convection and flow; and in imparting large-scale geochemical variations across the continental lithosphere (e.g. Rychert & Shearer, 2009; Tharimena et al., 2017). Constraining the 3D V_P/V_S structure on continental scales may provide information about the lateral distribution of melt-containing structures. Cognizant that we do not obtain consistently good resolution at the deepest LAB depths, which may exceed 200 km within cratonic regions (Artemieva, 2009; Jaupart et al., 1998; Jordan, 1975), we examine three regions within diverse tectonic settings which are associated with elevated V_P/V_S, and thus are candidates for the presence of melt.

In a local V_P tomography study probing the Yellowstone Hotspot, Farrell et al. (2014) use a 6% reduction in V_P, based on work by Hammond and Humphreys (2000), to infer the presence of partial melt. As V_P/V_S may be a more reliable indicator of melt, given the increased sensitivity of V_S to porous structures, we use a 2.0% $\delta(V_P/V_S)$ anomaly as a proxy for partial melt, also following Hammond and Humphreys (2000). This threshold appears to be less sensitive to variations in the geometry and connectivity of melt patches than either V_P or V_S. The extent of partial melt determined this way is likely underestimated, as the damping and smoothing imposed by the inversion result in a reduction of amplitude of the anomalies in our model, compared to the real Earth. A more quantitative interpretation of melt would need to correct for this effect; for the purposes of this exercise the damped model is sufficient.

Figure 13 shows three vertical cross-sections across regions associated with positive $\delta(V_P/V_S)$ anomalies. Section A-A' traverses the Columbia Plateau, the Yellowstone Hotspot, and extends into the Wyoming Craton. $\delta(V_P/V_S)$ is negative, and δV_S is positive, from the surface to ~70-80 km depth throughout the Columbia Plateau. This is similar to the inferred LAB depth of Hopper et al. (2014), who used Common Conversion Point stacking of Sp receiver functions. We therefore infer the low $\delta(V_P/V_S)$ layer to be the continental lithosphere. Below the Yellowstone Hotspot we see a continuous wedge-shaped positive V_P/V_S anomaly, interpreted as the upwelling Yellowstone Plume. East of this anomaly, negative $\delta(V_P/V_S)$ extends to depths greater than 100 km, and possibly as deep as 150 km, consistent with a thicker lithosphere below the Archean Wyoming Province (Foster et al., 2014; Hopper et al., 2014).

The highest $\delta(V_P/V_S)$ is found in the center of the Yellowstone anomaly, as a fairly thin, near-vertical feature. Here, at a depth around 60 km, the magnitude of $\delta(V_P/V_S)$ exceeds our 2% melt threshold. Huang et al. (2015) image several reservoirs of melt within the lithosphere (the largest at 30-50 km depth) and within the plume itself, abutting the base of the lithosphere at a depth of around 60 km. According to this interpretation, our melt anomaly is consistent with sublithospheric melting within the plume. Shallower melt patches may be below our limits of resolution, but it is clear that pervasive low δV_P and δV_S, and high $\delta(V_P/V_S)$, extend from below the lithosphere and are continuous through the entire lithosphere and that in these places melt is required by the seismic data.

In Section B-B', more variability is observed in the depth extent of the low V_P/V_S anomaly interpreted as the lithosphere. The lithosphere gradually thins to the southeast across the Basin and Range Province, then thickens below the Colorado Plateau, in agreement with imaging by Levander et al. (2011); Sine et al. (2008). It is thinnest at the boundary of the two provinces where it is underlain by high $\delta(V_P/V_S)$. $\delta(V_P/V_S)$ in fact exceeds 2.0% near 150 km depth, indicating that partial melt may be present near the base of the lithosphere at the western edge of the Colorado Plateau, consistent with Reid et al. (2012); Rudzitis et al. (2016). Similarly, the low-$\delta(V_P/V_S)$ layer is thinner and underlain by a higher $\delta(V_P/V_S)$ asthenosphere at the eastern boundary of the Plateau (near the Rio Grande Rift). Here, our inferred $\delta(V_P/V_S)$ does not exceed the 2% threshold to require melt, though melt may exist on scales too small to be resolvable through our inversion.

Finally, section C-C' extends from Western New York/Lake Ontario, through New England, and into the Atlantic. This section spans the low-velocity North Appalachian Anomaly (NAA) (Levin et al., 2017; Menke et al., 2016; Yang & Gao, 2018). The thick keel of the cratonic lithosphere is visible as a broad low-V_P/V_S anomaly which extends below 150 km depth. Thinning of the keel and increased $\delta(V_P/V_S)$ are observed below the topographic highs of the Adirondack and White Mountain ranges. This anomaly does match the approximate location of the NAA. $\delta(V_P/V_S)$ is not sufficiently high to invoke partial melt within this feature, but thinning of the lithosphere is consistent with passive convective upwelling at the edge of the North American craton (Levin et al., 2017; Menke et al., 2016). We lack the resolution to confirm whether a separate feature exists below the Adirondacks, as Yang and Gao (2018) suggest.

6 Conclusions

We have presented a workflow for determining multiple seismic properties via a joint inversion of multiple types of seismic data. Our inversion generates a model of δV_P and δV_S, but a novel application of this method is that it can be used to examine variations in the V_P/V_S ratio, which is influenced by elastic mineral properties as well as anelastic processes such as melting and attenuation. We have shown that 3D variations on the order of ∼3% exist within the North American continental lithosphere over scales of several hundreds of km.

We have also performed a clustering exercise using depth profiles of our model parameters. Spatial patterns of variation in δV_P, δV_S, and $\delta(V_P/V_S)$ are related to tectonic units, and in some cases these units share seismic characteristics with depth throughout the entire lithosphere. This indicates that structures present at the time of lithospheric assembly can shape the patterns of seismic anomalies observed today, and may influence the future evolution of the continental lithosphere.

Both δV_P and δV_S show a first-order pattern of low wavespeeds in the tectonically active Western US and high wavespeeds in the stable Eastern US, in agreement with decades of prior tomography work. This contrast between the Eastern and Western United States does not dominate the $\delta(V_P/V_S)$ maps in the upper 60 km, where the highest V_P/V_S excursions are observed below regions such as Yellowstone and the margins of the Colorado Plateau. At 80 km depth and below, though, the east-to-west pattern dominates $\delta(V_P/V_S)$, with negative values found in the East and positive in the West. As the base of the lithosphere may be found at 80 km depth or shallower over much of the Western US (e.g. Hopper & Fischer, 2018; Yuan et al., 2011), there we image the warmer, less viscous, and therefore strongly seismically anomalous, asthenosphere. We conclude that the first-order $\delta(V_P/V_S)$ patterns are primarily sensitive to melt and asthenosphere-lithosphere interactions.

Xenolith evidence indicates that the cratonic lithosphere imaged in the Eastern US at the depths considered here may be chemically depleted (Boyd, 1989; O'Reilly & Griffin, 2006; Saltzer et al., 2001) and/or have experienced widespread metasomatic alteration (Boyd, 1989; Kelemen et al., 1998). The distinct seismic character of the Eastern US may therefore have a geochemical component. Our joint derivation of δV_P and $\delta(V_P/V_S)$ provides a tool to probe these changes in mineral composition, as V_P/V_S is sensitive to elastic properties in a different way than V_P or V_S alone. By constraining a diversity of seismic properties, combined with thermodynamic modeling of petrologic information, the thermal and compositional causes of seismic heterogeneity can be understood and distinguished. This topic will be the subject of future work.

Acknowledgments
The authors would like to acknowledge several sources for the seismic data used in this study. Body wave arrival time data can be found in the IRIS Data Management Center (*ds.iris. edu/ds/nodes/dmc/data/*) and the ISC-EHB Bulletin (*isc.ac.uk/isc-ehb/search/arrivals/*). Further information on accessing the Rayleigh wave phase velocity measurements can be found in the following references: Ekström (2017); Foster et al. (2020); Petrescu et al. (2017); Schaeffer and Lebedev (2014). Model MITPS_20 will be made publicly available via the IRIS Earth Model Center (EMC). We thank Alistair Boyce, Laura Petrescu, Anna Foster, Fiona Darbyshire, and Andrew Frederiksen for their collaboration and their generosity in sharing data. We also thank the associate editor and an anonymous reviewer for their feedback and suggestions, which have improved this manuscript.

References

Abt, D. L., Fischer, K. M., French, S. W., Ford, H. A., Yuan, H., & Romanowicz, B. (2010). North American lithospheric discontinuity structure imaged by *Ps* and *Sp* receiver functions. *J. Geophys. Res.*, *115*(B9).

Afonso, J. C., Ranalli, G., Fernández, M., Griffin, W. L., O'Reilly, S. Y., & Faul, U. (2010). On the Vp/Vs-Mg# correlation in mantle peridotites: Implications for the identification of thermal and compositional anomalies in the upper mantle. *Earth Planet. Sci. Lett.*, *289*, 606-618.

Aki, K., & Lee, W. H. K. (1976). Determination of three-dimensional velocity anomalies under a seismic array using first P arrival times from local earthquakes 1. A homogeneous initial model. *J. Geophys. Res.*, *81*, 4381-4399.

Artemieva, I. M. (2009). The continental lithosphere: reconciling thermal, seismic, and petrologic data. *Lithos*, *109*(1-2), 23-46.

Baptiste, V., & Tommasi, A. (2014). Petrophysical constraints on the seismic properties of the Kaapvaal craton mantle root. *Solid Earth*, *5*, 45-63.

Bedle, H., & van der Lee, S. (2009). S velocity variations beneath North America. *J. Geophys. Res.*, *114*.

Bernardino, M. V., Jones, C. H., Levandowski, W., Bastow, I., Owens, T. J., & Gilbert, H. (2019). A multicomponent Isabella anomaly: Resolving the physical state of the Sierra Nevada upper mantle from Vp/Vs anisotropy tomography. *Geosphere*, *15*(6), 2018-2042.

Blackwell, D., Richards, M., Frone, Z., Batir, J., Ruzo, A., Dingwall, R., & Williams, M. (2011). Temperature-At-Depth Maps for the Conterminous U. S. and Geothermal Resource Estimates. *GRC Transactions*, *35*, 1545-1550.

Boyce, A., Bastow, I. D., Darbyshire, F. A., Ellwood, A. G., Gilligan, A., Levin, V., & Menke, W. (2016). Subduction beneath Laurentia modified the eastern North American cratonic edge: Evidence from P wave and S wave tomography.

Journal Geophys. Res., *121*(7), 5013-5030.

Boyce, A., Bastow, I. D., Rondenay, S., & van der Hilst, R. D. (2017). From Relative to Absolute Teleseismic Travel Times: The Absolute Arrival-Time Recovery Method (AARM). *Bull. Seism. Soc. Am.*, *107*(5), 2511-2520.

Boyd, F. R. (1989). Compositional distinction between oceanic and cratonic lithosphere. *Earth Planet. Sci. Lett.*, *96*(1-2), 15-26.

Burdick, S., Li, C., Martynov, V., Cox, T., Eakins, J., Mulder, T., ... van der Hilst, R. D. (2008). Upper mantle heterogeneity beneath North America from travel time tomography with global and USArray Transportable Array data. *Seis. Res. Lett.*, *79*, 384-392.

Burdick, S., Vernon, F. L., Martynov, V., Eakins, J., Cox, T., Tytell, J., ... van der Hilst, R. D. (2017). Model Update May 2016: Upper mantle heterogeneity beneath North America from travel time tomography with global and USArray data. *Seis. Res. Lett.*, *85*, 77-81.

Chantel, J., Manthilake, G., Andrault, D., Novella, D., Yu, T., & Wang, Y. (2016). Experimental evidence supports mantle partial melting in the asthenosphere. *Sci. Adv.*, *2*, 1-7.

Chevrot, S., & van der Hilst, R. D. (2000). The Poisson ratio of the Australian crust: geological and geophysical implications. *Earth Planet. Sci. Lett.*, *183*, 121-132.

Christensen, N. I., & Mooney, W. D. (1995). Seismic velocity structure and composition of the continental crust: A global view. *J. Geophys. Res.*, *100*(B6), 9761-9788.

Darbyshire, F. A., Eaton, D. W., & Bastow, I. D. (2013). Seismic imaging of the lithosphere beneath Hudson Bay: Episodic growth of the Laurentian mantle keel. *Earth Planet. Sci. Lett.*, *373*, 179-193.

Eberhart-Phillips, D., & Fry, B. (2017). A new scheme for joint surface wave and earthquake travel-time inversion and resulting 3-D velocity model for the western North Island, New Zealand. *Phys. Earth Planet. Int.*, *269*, 98-111.

Ekström, G. (2017). Short-period surface-wave phase velocities across the coterminous United States. *Phys. Earth Planet. Int.*, *270*, 168-175.

Engdahl, E. R., van der Hilst, R., & Buland, R. (1998). Global teleseismic earthquake relocation with improved travel times and procedures for depth determination. *Bull. Seism. Soc. Am.*, *88*, 722-743.

Eymold, W. T., & Jordan, T. H. (2019). Tectonic regionalization of the southern california crust from tomographic cluster analysis. *J. Geophys. Res.*, *124*, 11,840-11,865.

Fang, H., Yao, H., Zhang, H., Huang, Y., & van der Hilst, R. D. (2015). Direct inversion of surface wave dispersion for three-dimensional shallow crustal structure based on ray tracing: methodology and application. *Geophys. J. Int.*, *201*, 1251-1263.

Fang, H., Yao, H., Zhang, H., Thurber, C., Ben-Zion, Y., & van der Hilst, R. D. (2019). Vp/Vs tomography in the southern California plate boundary region using body and surface wave traveltime data. *Geophys. J. Int.*, *216*, 609-620.

Fang, H., Zhang, H., Yao, H., Allam, A., Zigone, D., Ben-Zion, Y., ... van der Hilst, R. D. (2016). A new algorithm for three-dimensional joint inversion of body wave and surface wave data and its application to the Southern California plate boundary region. *J. Geophys. Res.*, *121*, 3557-3569.

Farrell, J., Smith, R. B., Husen, S., & Diehl, T. (2014). Tomography from 26 years of seismicity revealing that the spatial extent of the Yellowstone crustal magma reservoir extends well beyond the Yellowstone caldera. *Geophys. Res. Lett.*, *41*, 3068-3073.

Faul, U. H., & Jackson, I. (2005). The seismological signature of temperature and grain size variations in the upper mantle. *Earth Planet. Sci. Lett.*, *234*, 119-134.

Fichtner, A., Kennett, B. L. N., Igle, H., & Bunge, H. (2009). Full seismic waveform tomography for upper-mantle structure in the Australasian region using adjoint methods. *Geophys. J. Int.*, *179*, 1703-1725.

Foster, A., Darbyshire, F. A., & Schaeffer, A. (2020). Anisotropic structure of the central North American Craton surrounding the Mid-Continent Rift: Evidence from Rayleigh waves. *Precamb. Res.*, *342*.

Foster, K., Dueker, K., Schmandt, B., & Yuan, H. (2014). A sharp cratonic lithosphere-asthenosphere boundary beneath the American Midwest and its relation to mantle flow. *Earth Planet. Sci. Lett.*, *402*, 82-89.

Goes, S., & van der Lee, S. (2002). Thermal structure of the North American uppermost mantle inferred from seismic tomography. *J. Geophys. Res.*, *107*(B3), 1-13.

Golos, E. M., Fang, H., Yao, H., Zhang, H., Burdick, S., Vernon, F., . . . van der Hilst, R. D. (2018). Shear wave tomography beneath the United States using a joint inversion of surface and body waves. *J. Geophys. Res.*, *123*, 5169-5189.

Hammond, W. C., & Humphreys, E. D. (2000). Upper mantle seismic velocity: Effects of realistic partial melt geometries. *J. Geophys. Res.*, *105*(B5), 10975-10986.

Hejrani, B., Balling, N., Jacobsen, B. H., & Tilmann, F. (2015). Upper-mantle P-and S-wave velocities across the Northern Tornquist Zone from traveltime tomography. *Geophys. J. Int.*, *203*(1), 437-458.

Herrmann, R. B. (2013). Computer programs in seismology: An evolving tool for instruction and research. *Seism. Res. Lettr.*, *84*, 1081-1088.

Hopper, E., & Fischer, K. (2018). The changing face of the Lithosphere-Asthenosphere Boundary: Imaging continental scale patterns in upper mantle structure across the contiguous U.S. with Sp converted waves. *Geochem., Geophys., Geosyst.*, *19*(8), 2593-2614.

Hopper, E., Ford, H. A., Fischer, K. M., & Lekic, V. (2014). The lithosphereasthenosphere boundary and the tectonic and magmatic history of the northwestern United States. *Earth Planet. Sci. Lett.*, *402*, 69-81.

Huang, H.-H., Lin, F.-C., Schmandt, B., Farrell, J., Smith, R. B., & Tsai, V. C. (2015). The Yellowstone magmatic system from the mantle plume to the upper crust. *Science*, *384*, 773-776.

Humphreys, E., Hessler, E., Dueker, K., Farmer, G. L., Erslev, E., & Atwater, T. (2003). How Laramide-Age Hydration of North American Lithosphere by the Farallon Slab Controlled Subsequent Activity in the Western United States. *Int. Geol. Rev.*, *45*(7), 575-595.

Jaupart, C., Mareschal, J.-C., Bouquerel, H., & Phaneuf, C. (2014). The building and stabilization of an Archean Craton in the Superior Province, Canada, from a heat flow perspective. *J. Geophys. Res.*, *119*, 9130-9155.

Jaupart, C., Mareschal, J. C., Guillou-Frottier, L., & Davaille, A. (1998). Heat flow and thickness of the lithosphere in the Canadian Shield. *J. Geophys. Res.*, *103*(B7), 15,269-15,286.

Jordan, T. H. (1975). The continental tectosphere. *Rev. Geophys.*, *13*(3), 1-12.

Jordan, T. H. (1988). Structure and formation of the continental tectosphere. *J. Petrology*, *1*, 11-37.

Kaban, M. K., Tesauro, W. D., & Cloetingh, S. A. P. L. (2014). Density, temperature, and composition of the North American lithosphere: New insights from a joint analysis of seismic, gravity, and mineral physics data: 1. Density structure of the crust and upper mantle. *Geochem., Geophys., Geosyst.*, *15*, 4781-4807.

Karato, S.-I., & Karki, B. B. (2001). Origin of lateral variation of seismic wave velocities and density in the deep mantle. *J. Geophys. Res.*, *106*, 21771-21783.

Kelemen, P. B., Hart, S. R., & Bernstein, S. (1998). Silica enrichment in the continental upper mantle via melt/rock reaction. *Earth Planet. Sci. Lett.*, *164*, 387-

406.
Kennett, B. L. N., Engdahl, E. R., & Buland, R. (1995). Constraints on seismic velocities in the Earth from traveltimes. *Geophys. J. Int.*, *122*, 108-124.
Kennett, B. L. N., Widiyantoro, S., & van der Hilst, R. D. (1998). Joint seismic tomography for bulk sound and shear wave speed in the Earth's mantle. *J. Geophys. Res.*, *103*(B6), 12,469-12,493.
Khan, A., Zunino, A., & Deschamps, F. (2011). The thermo-chemical and physical structure beneath the North American continent from Bayesian inversion of surface-wave phase velocities. *J. Geophys. Res.*, *116*(B9), 1-23.
Krauss, Z., & Menke, W. (2020). The Northern Gulf Anomaly: P- and S-wave travel time delays illuminate a strong thermal feature beneath the Northern Gulf of Mexico. *Earth Planet. Sci. Lett.*, *534*.
Lee, C.-T. A. (2003). Compositional variation of density and seismic velocities in natural peridotites at STP conditions: Implications for seismic imaging of compositional heterogeneities in the upper mantle. *J. Geophys. Res.*, *108*, 1-20.
Levander, A., Schmandt, B., Miller, M. S., Liu, K., Karlstrom, K. E., Crow, R. S., … Humphreys, E. D. (2011). Continuing colorado plateau uplift by delamination-style convective lithospheric downwelling. *Nature*, *472*, 461-465.
Lévěque, J. J., Rivera, L., & Wittlinger, G. (1993). On the use of the checker-board test to assess the resolution of tomographic inversions. *Geophys. J. Int.*, *115*, 313-318.
Levin, V., Long, M. D., Skryzalin, P., Li, Y., & López, I. (2017). Seismic evidence for a recently formed mantle upwelling beneath New England. *Geology*, *46*, 87-90.
Li, C., van der Hilst, R. D., Engdahl, E. R., & Burdick, S. (2008). A new global model for P wave speed variations in Earth's mantle. *Geochem. Geophys. Geosyst.*, *9*.
Ma, X., & Lowry, A. R. (2017). USArray Imaging of Continental Crust in the Conterminous United States. *Tectonics*, *36*, 2882-2902.
Mancinelli, N. J., Fischer, K. M., & Dalton, C. A. (2017). How Sharp Is the Cratonic Lithosphere-Asthenosphere Transition? *Geophys. Res. Lett.*, *44*(20), 10,189-10,197.
Masters, G., Laske, G., Bolton, H., & Dziewonski, A. (2000). The relative behavior of shear velocity, bulk sound speed, and compressional velocity in the mantle: implications for chemical and thermal structure. In S. Karato, A. Forte, R. Liebermann, G. Masters, & L. Stixrude (Eds.), *Earth's Deep Interior: Mineral Physics and Tomography From the Atomic to the Global Scale, Volume 117* (p. 63-87). AGU.
Menke, W., Skryzalin, P., Levin, V., Harper, T., Darbyshire, F., & Dong, T. (2016). The Northern Appalachian Anomaly: A modern asthenospheric upwelling. *Geophys. Res. Lett.*, *43*(19), 10173-10179.
Obrebski, M., Allen, R. M., Pollitz, F., & Hung, S.-H. (2011). Lithosphere-asthenosphere interaction beneath the western United States from the joint inversion of body-wave travel times and surface-wave phase velocities. *Geophys. J. Int.*, *185*, 1003-1021.
O'Reilly, S. Y., & Griffin, W. L. (2006). Imaging global chemical and thermal heterogeneity in the subcontinental lithospheric mantle with garnets and xenoliths: Geophysical implications. *Tectonophys.*, *416*(1-4), 289-309.
Patiño Douce, A. E., Humphreys, E. D., & Johnston, A. D. (1990). Anatexis and metamorphism in tectonically thickened continental crust exemplified by the sevier hinterland, western north america. *Earth Planet. Sci. Lett.*, *97*(3-4), 290-315.
Perry, H. K. C., Forte, A. M., & Eaton, D. W. S. (2003). Upper-mantle thermochemical structure below North American from seismic-geodynamic flow

models. *Geophys. J. Int.*, *154*(2), 279-299.

Petrescu, L., Darbyshire, F., Bastow, I., Totten, E., & Gilligan, A. (2017). Seismic anisotropy of Precambrian lithosphere: Insights from Rayleigh wave tomography of the eastern Superior Craton. *J. Geophys. Res.*, *122*(5), 3754-3775.

Pollack, H. N. (1986). Cratonization and thermal evolution of the mantle. *Earth Planet. Sci. Lett.*, *80*, 175-182.

Porritt, R. W., Allen, R. M., & Pollitz, F. F. (2014). Seismic imaging east of the Rocky Mountains with USArray. *Earth Planet. Sci. Lett.*, *402*, 16-25.

Porter, R., Liu, Y., & Holt, W. E. (2016). Lithospheric records of orogeny within the continental U.S. *Geophys. Res. Lett.*, *43*(1), 144-153.

Priestley, K., & Tilmann, F. (2009). Relationship between the upper mantle high velocity seismic lid and the continental lithosphere. *Lithos*, *109*(1-2), 112-124.

Purevsuren, U. (2014). *Crustal thickness and Vp/Vs beneath the Western United States: Constraints from stacking of receiver functions* (Unpublished doctoral dissertation). Missouri Univ. Sci. Tech.

Ramesh, D. S., Kind, R., & Yuan, X. (2002). Receiver function analysis of the North American crust and upper mantle. *Geophys. J. Int.*, *150*, 91-108.

Rawlinson, N., & Fishwick, S. (2012). Seismic structure of the southeast Australian lithosphere from surface and body wave tomography. *Tectonophysics*, *572-573*, 111-122.

Reid, M. R., Bouchet, R. A., Blichert-Toft, J., Levander, A., Liu, K., Miller, M. S., & Ramos, F. C. (2012). Melting under the Colorado Plateau, USA. *Geology*, *40*(5), 387-390.

Rocker, S., Thurber, C., Roberts, K., & Powell, L. (2006). Refining the image of the San Andreas Fault near Parkfield, California using a finite difference travel time computation technique. *Tectonophys.*, *426*(1-2), 189-205.

Rudzitis, S., Reid, M. R., & Blichert-Toft, J. (2016). On edge melting under the Colorado Plateau margin. *Geochem., Geophys., Geosyst.*, *17*(7), 2835-2854.

Rychert, C. A., & Shearer, P. M. (2009). A global view of the lithosphere-asthenosphere boundary. *Science*, *324*(5926), 495-498.

Saltzer, R. L., Chatterjee, N., & Grove, T. L. (2001). The spatial distribution of garnets and pyroxenes in mantle from peridotites: pressure-temperature history of peridotites from the Kaapvaal Craton. *J. Petrology*, *42*(12), 2215-2229.

Schaeffer, A. J., & Lebedev, S. (2014). Imaging the North American continent using waveform inversion of global and USArray data. *Earth Planet. Sci. Lett.*, *402*, 26-41.

Schmandt, B., & Humphreys, E. (2010). Complex subduction and small-scale convection revealed by body-wave tomography of the western United States upper mantle. *Earth Planet. Sci. Lett.*, *297*, 435-445.

Schmandt, B., & Lin, F.-C. (2014). P and S wave tomography of the mantle beneath the United States. *Geophys. Res. Lett.*, *41*, 6342-6349.

Schmandt, B., Lin, F.-C., & Karlstrom, K. E. (2015). Distinct crustal isostasy trends east and west of the Rocky Mountain Front. *Geophys. Res. Lett.*, *42*, 10,290-10,298.

Schulz, K. J., & Cannon, W. F. (2007). The Penokean orogeny in the Lake Superior region. *Precambrian Res.*, *157*(1-4), 4-25.

Schutt, D. L., & Lesher, C. E. (2006). Effects of melt depletion on the density and seismic velocity of garnet and spinel lherzolite. *J. Geophys. Res.*, *111*(5).

Schutt, D. L., & Lesher, C. E. (2010). Compositional trends among Kaapvaal Craton garnet peridotite xenoliths and their effects on seismic velocity and density. *Earth Planet. Sci. Lett.*, *300*, 367-373.

Schutt, D. L., Lowry, A. R., & Buehler, J. S. (2018). Moho temperature and mobility of lower crust in the western United States. *Geology*, *46*(3), 219-222.

Shen, W., & Ritzwoller, M. H. (2016). Crustal and uppermost mantle structure beneath the United States. *J. Geophys. Res.*, *121*, 4306-4342.

Shillington, D. J., van Avendonk, H. J. A., Behn, M. D., Kelemen, P. B., & Jagoutz, O. (2013). Constraints on the composition of the Aleutian arc lower crust from VP/VS. *Geophys. Res. Lett.*, *40*, 2579-2584.

Silver, P. G., Meyer, R. P., & James, D. E. (1993). Intermediate-scale observations of the Earth's deep interior from the APT89 transportable teleseismic experiment. *Geophys. Res. Lett.*, *20*(12), 1123-1126.

Simons, F. J., Zielhaus, A., & vand der Hilst, R. D. (1999). The Deep Structure of the Australian Continent from Surface-Wave Tomography. *Devel. Geotectonics*, *24*, 17-43.

Sine, C. R., Wilson, D., Gao, W., Grand, S. P., Aster, R., Ni, J., & Baldridge, W. S. (2008). Mantle structure beneath the western edge of the Colorado Plateau. *Geophys. Res. Lett.*, *35*(10).

Spakman, W., & Nolet, G. (1988). Imaging algorithms, accuracy and resolution in delay time tomography [Chapter]. In N. J. Vlaar, G. Nolet, M. R. J. Wortel, & S. A. P. L. Cloetingh (Eds.), *Mathematical Geophysics: A Survey of Recent Developments in Seismology and Geodynamics* (p. 155-187). Dordrecht: D. Reidel.

Stein, S., Stein, C. A., Elling, R., Kley, J., Keller, G. R., Wysession, M., ... Moucha, R. (2018). Insights from North America's failed Midcontinent Rift into the evolution of continental rifts and passive continental margins. *Tectonophys.*, *744*, 403-421.

Szwillus, W., Afonso, J. C., Ebbing, J., & Mooney, W. D. (2019). Global crustal thickness and velocity structure from geostatistical analysis of seismic data. *J. Geophys. Res.*, *124*(2), 1626-1652.

Takei, Y. (2002). Effect of pore geometry on V_P/V_S: from equilibrium geometry to crack. *J. Geophys. Res.*, *107*(B2).

Takei, Y. (2017). Effects of Partial Melting on Seismic Velocity and Attenuation: A New Insight from Experiments. *Ann. Rev. Earth Planet. Sci.*, *45*, 447-470.

Tesoniero, A., Auer, L., Boschi, L., & Cammarano, F. (2015). Hydration of marginal basins and compositional variations within the continental lithospheric mantle inferred from a new global model of shear and compressional velocity. *J. Geophys. Res.*, *120*, 7789-7813.

Tharimena, S., Rychert, C., & Harmon, N. (2017). A unified continental thickness from seismology and diamonds suggests a melt-defined plate. *Science*, *357*(6351), 580-583.

Thurber, C. H., Atre, S. R., & Eberhart-Phillips, D. (1995). Three-dimensional Vp and Vp/Vs structure at Loma Prieta, California, from local earthquake tomography. *Geophys. Res. Lett.*, *22*(22), 3079-3082.

Trampert, J., Vacher, P., & Vlaar, N. (2001). Sensitivities of seismic velocities to temperature, pressure and composition in the lower mantle. *Phys. Earth Planet. Int.*, *124*, 255-267.

van der Hilst, R. D., Engdahl, E. R., & Spakman, W. (1993). Tomographic inversion of P and pP data for aspherical mantle structure beneath the northwest Pacific region. *Geophys. J. Int.*, *115*, 264-302.

van Schmus, W. R., & Bickford, M. E. (1981). Chapter 11 Proterozoic Chronology and Evolution of the Midcontinent Region, North America. In A. Kröner (Ed.), *Precambrian Plate Tectonics* (Vol. 4, p. 261-296). Elsevier.

Wagner, L., Anderson, M. L., Jackson, J. M., Beck, S. L., & Zandt, G. (2008). Seismic evidence for orthopyroxene enrichment in the continental lithosphere. *Geology*, *36*(12), 935-938.

Wang, Y., Forsyth, D. W., Rau, C. J., Carriero, N., Schmandt, B., Gaherty, J. B., & Savage, B. (2013). Fossil slabs attached to unsubducted fragments of the Farallon plate. *Proc. Nat. Academy Sci.*, *110*(14), 5342-5346.

Wei, Z., Kennett, B. L. N., & Sun, W. (2018). Sn-wave velocity structure of the uppermost mantle beneath the Australian continent. *Geophys. J. Int.*, *213*, 2071-

2084.

Whitmeyer, S. J., & Karlstrom, K. E. (2007). Tectonic model for the Proterozoic growth of North America. *Geosphere*, *3*(4), 220-259.

Yang, X., & Gao, H. (2018). FullWave Seismic Tomography in the Northeastern United States: New Insights Into the Uplift Mechanism of the Adirondack Mountains. *Geophys. Res. Lett.*, *45*(12), 5992-6000.

Yang, X., Pavlis, G. L., Hamburger, M. W., Marshak, S., Gilbert, H., Rupp, J., ... Carpenter, N. S. (2017). Detailed crustal thickness variations beneath the Illinois Basin area: Implications for crustal evolution of the midcontinent. *J. Geophys. Res.*, *122*, 6323-6345.

Yuan, H., Romanowicz, B., Fischer, K. M., & Abt, D. (2011). 3-D shear wave radially and azimuthally anisotropic velocity model of the North American upper mantle. *Geophys. J. Int.*, *184*, 1237-1260.

Zandt, G., Myers, S. C., & Wallace, T. C. (1995). Crust and mantle structure across the Basin and Range- Colorado Plateau boundary at 37°N latitude and implications for Cenozoic extensional mechanism. *J. Geophys. Res.*, *100*(B6), 10,529-10,548.

Zhang, H., van der Lee, S., Wolin, E., Bollmann, T. A., Revenaugh, J., Wiens, D. A., ... Jurdy, D. M. (2016). Distinct crustal structure of the North American Midcontinent Rift from P wave receiver functions. *J. Geophys. Res.*, *121*, 8136-8153.

Zhu, H., Komatitsch, D., & Tromp, J. (2017). Radial anisotropy of the North American upper mantle based on adjoint tomography with USArray. *Geophys. J. Int.*, *211*, 349-377.

Zhu, L., & Kanamori, H. (2000). Moho depth variation in southern California from teleseismic receiver functions. *J. Geophys. Res.*, *105*(B2), 2969-2980.

Figure 1.

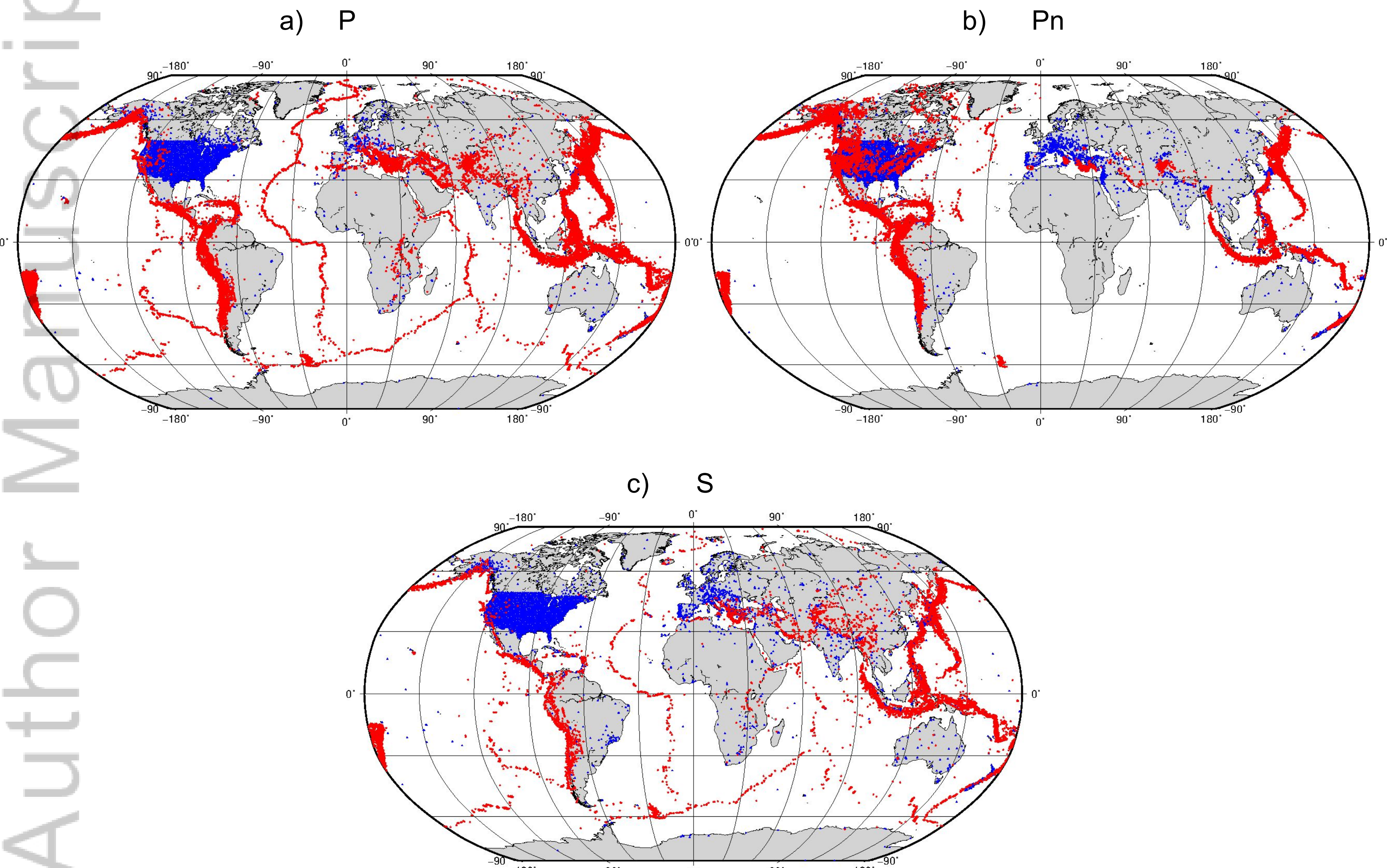

a) P
b) Pn
c) S
−180°
−90°
0°
90°
180°
90°
−90°
0°

Figure 2.

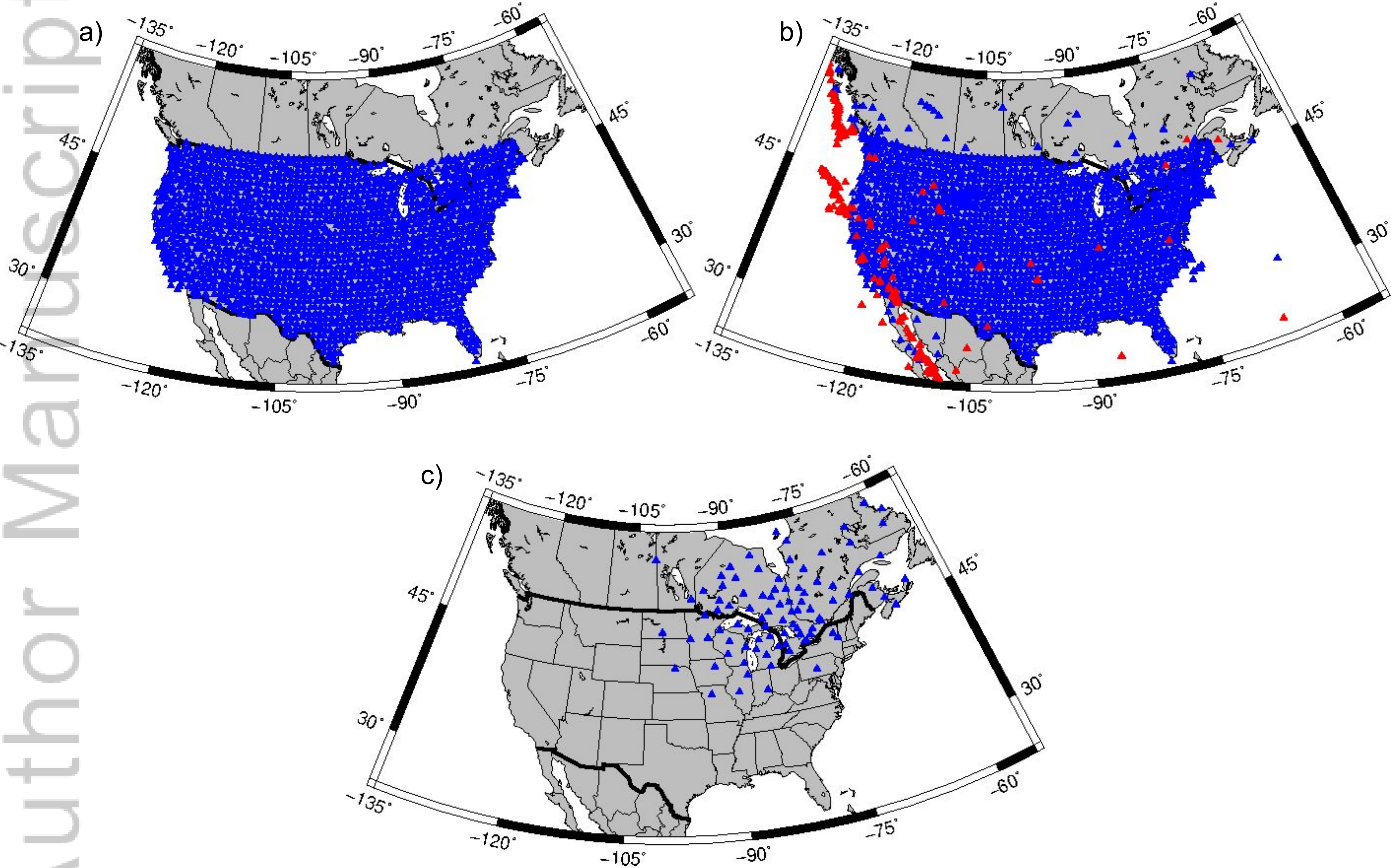
a)
−135°
−120°
−105°
−90°
−75°
−60°
45°
30°
b)
−135°
−120°
−105°
−90°
−75°
−60°
45°
30°
c)
−135°
−120°
−105°
−90°
−75°
−60°
45°
30°

Figure 3.

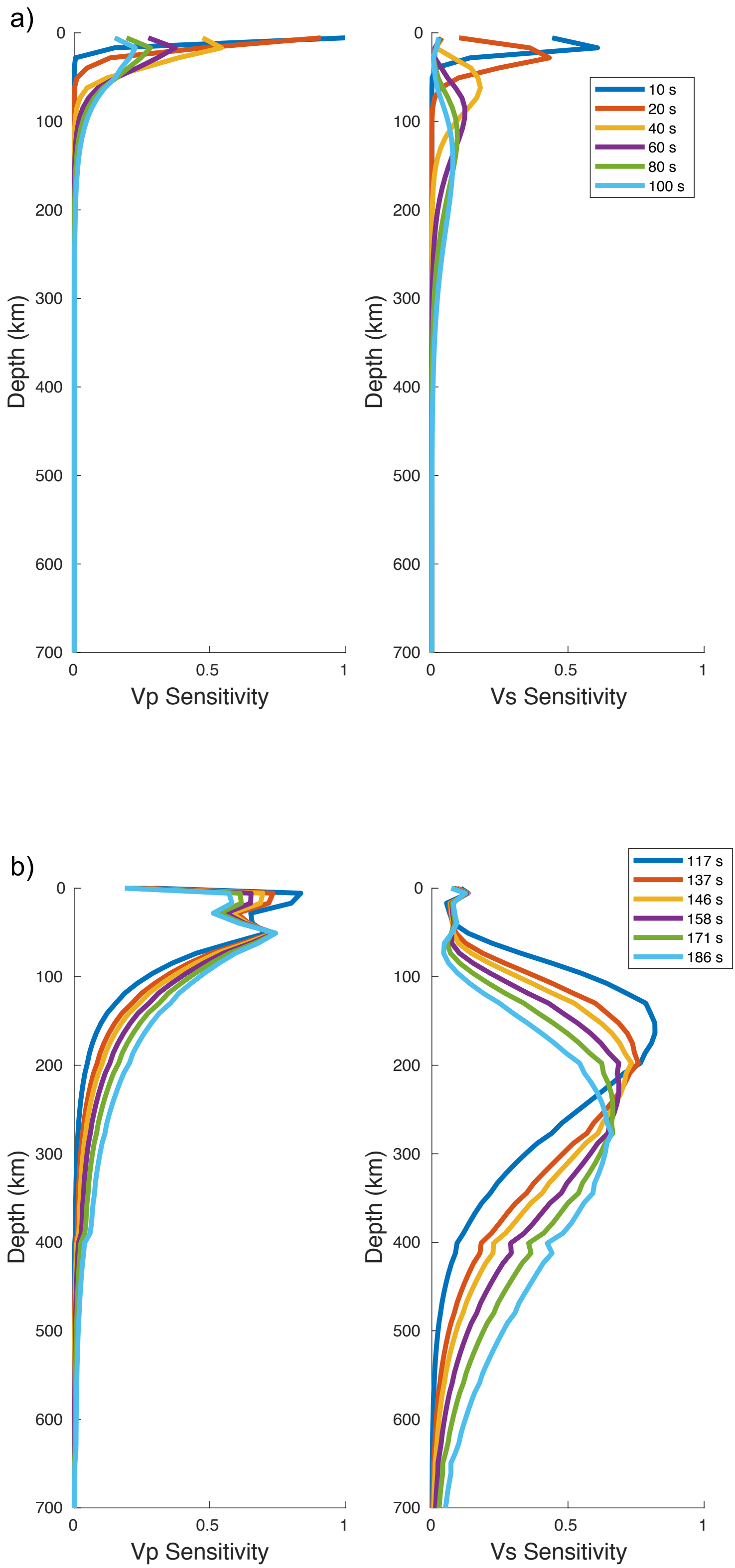

a)
b)
Depth (km)
Vp Sensitivity
Vs Sensitivity
0
100
200
300
400
500
600
700
0
0.5
1
10 s
20 s
40 s
60 s
80 s
100 s
117 s
137 s
146 s
158 s
171 s
186 s

Figure 4.

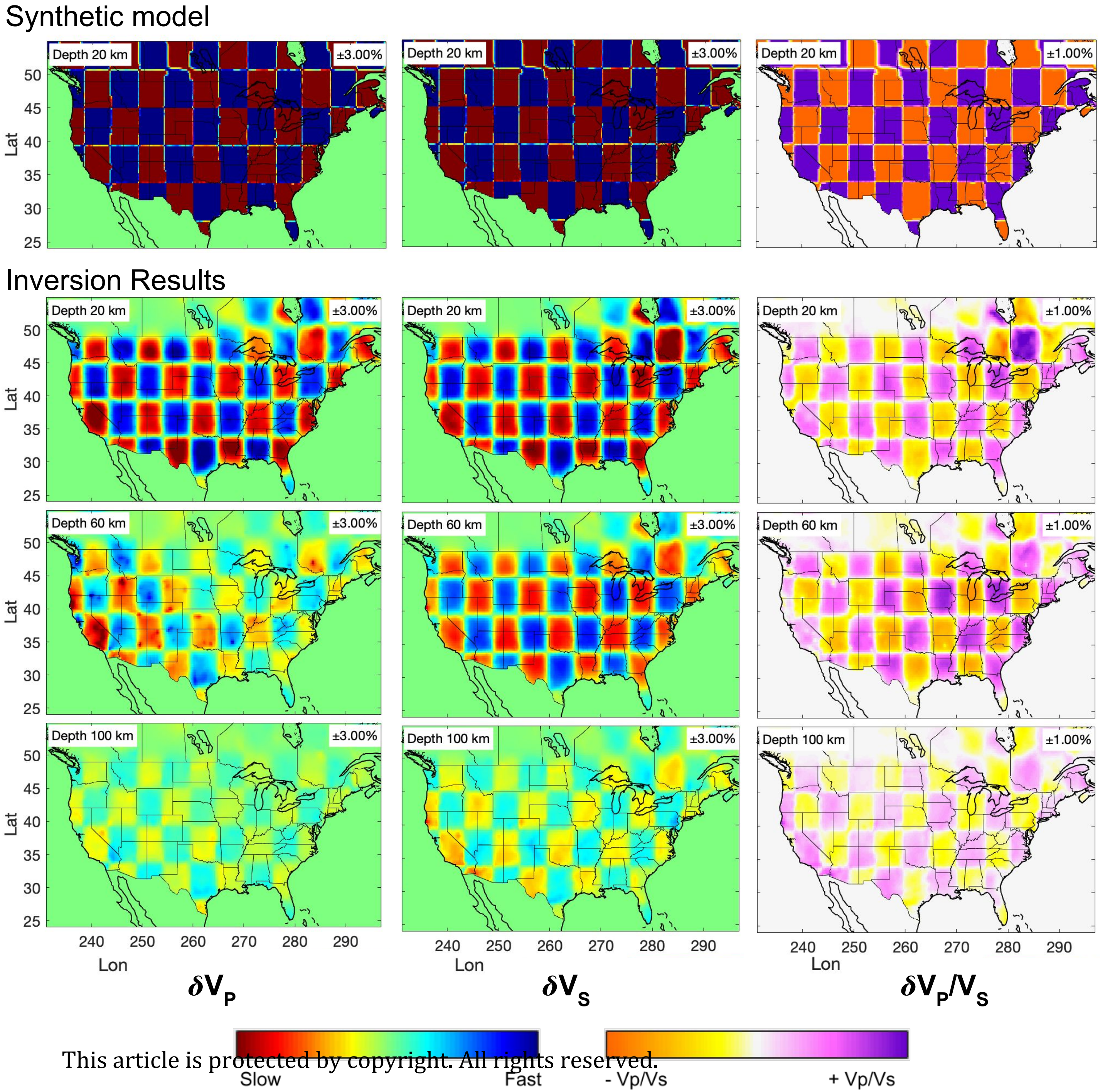

Synthetic model
Inversion Results
Depth 20 km
Depth 60 km
Depth 100 km
±3.00%
±1.00%
Lat
50
45
40
35
30
25
Lon
240
250
260
270
280
290
δVP
δVS
δVP/VS
Slow
Fast
- Vp/Vs
+ Vp/Vs

Figure 5.

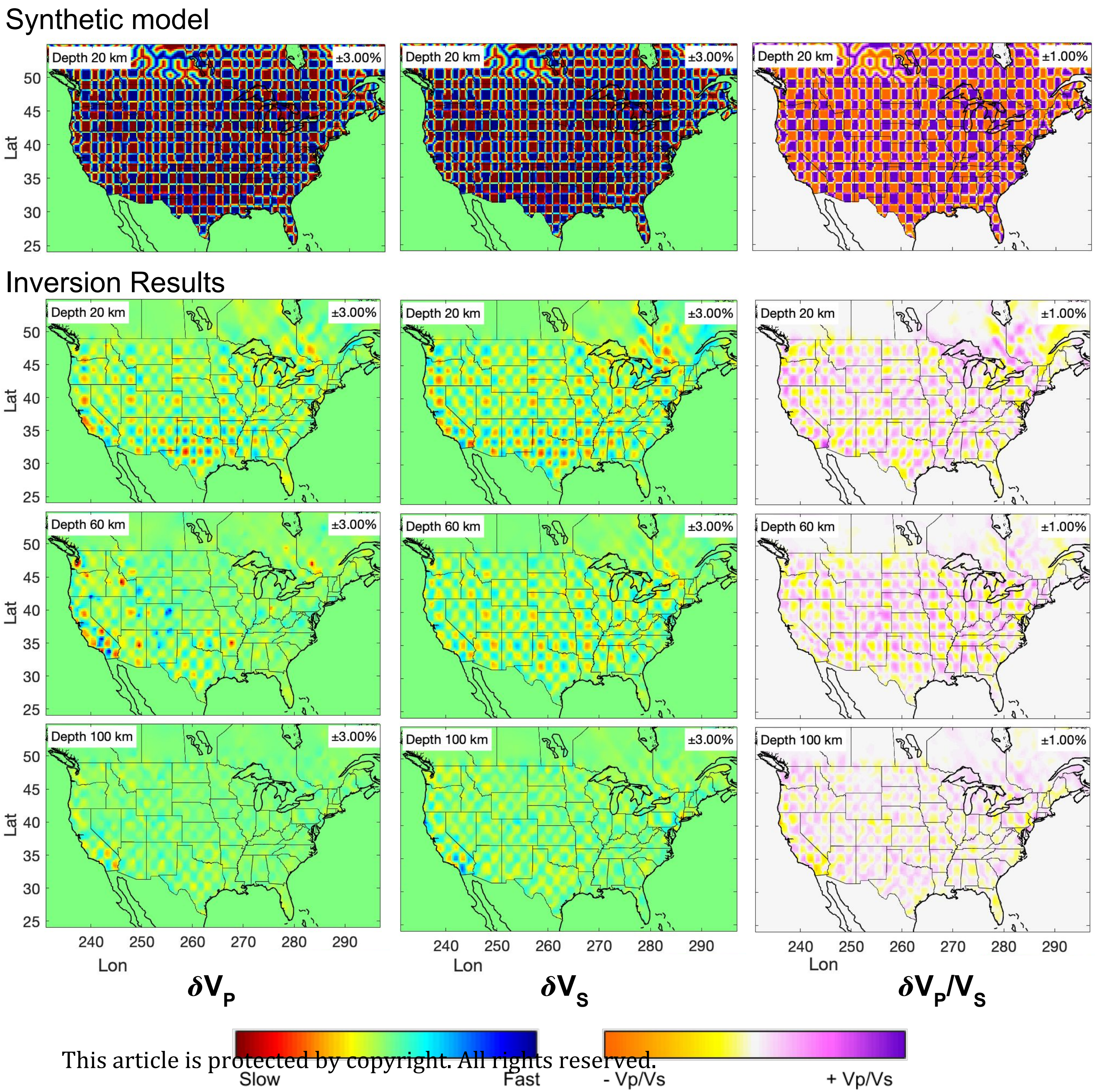

Synthetic model
Inversion Results
Depth 20 km
Depth 60 km
Depth 100 km
±3.00%
±1.00%
Lat
Lon
δVP
δVS
δVP/VS
Slow
Fast
- Vp/Vs
+ Vp/Vs

Figure 6.

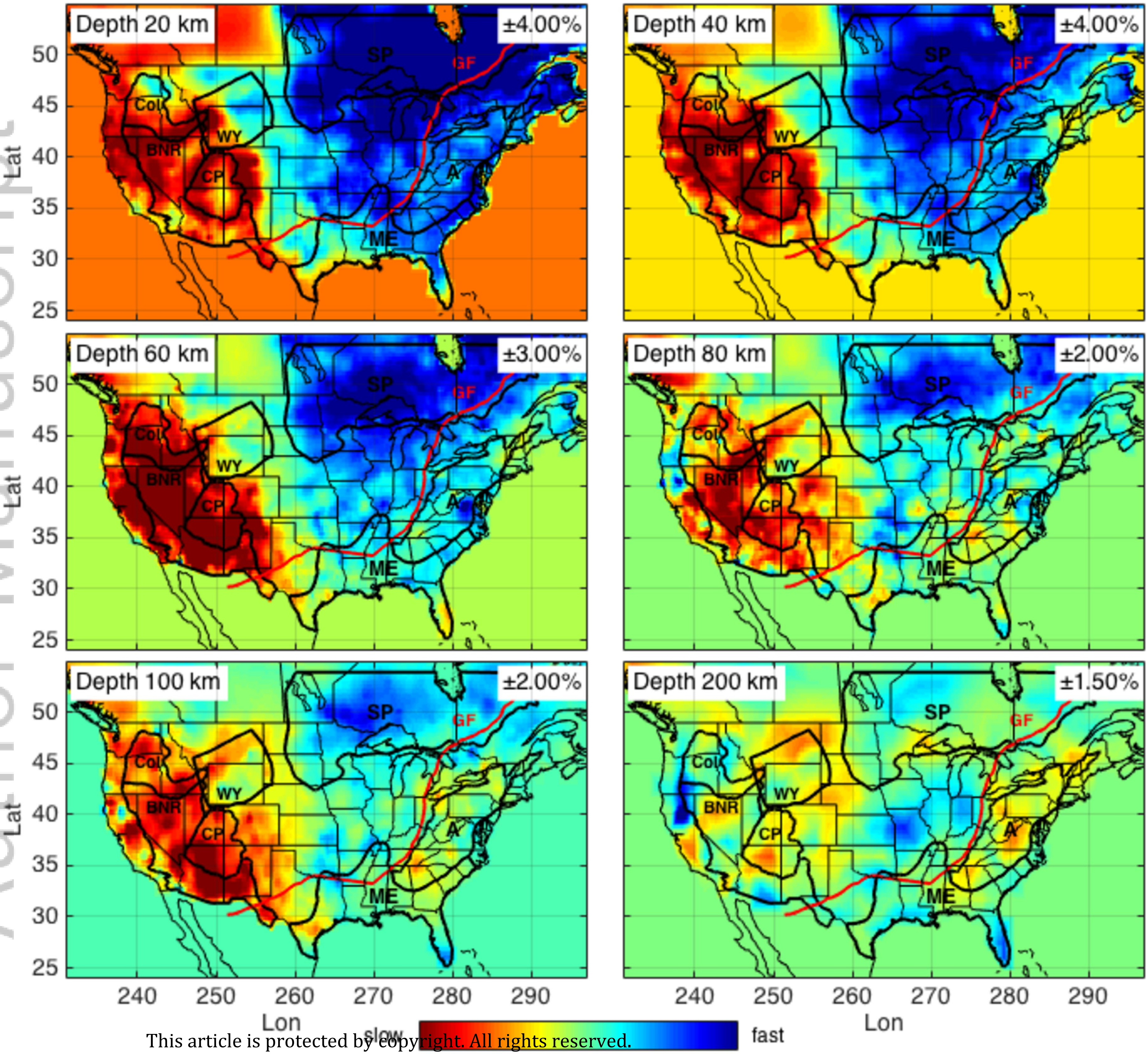
Depth 20 km
±4.00%
Depth 40 km
±4.00%
Depth 60 km
±3.00%
Depth 80 km
±2.00%
Depth 100 km
±2.00%
Depth 200 km
±1.50%
SP
GF
Col
WY
BNR
CP
A
ME
Lat
Lon
240
250
260
270
280
290
25
30
35
40
45
50
slow
fast

Figure 7.

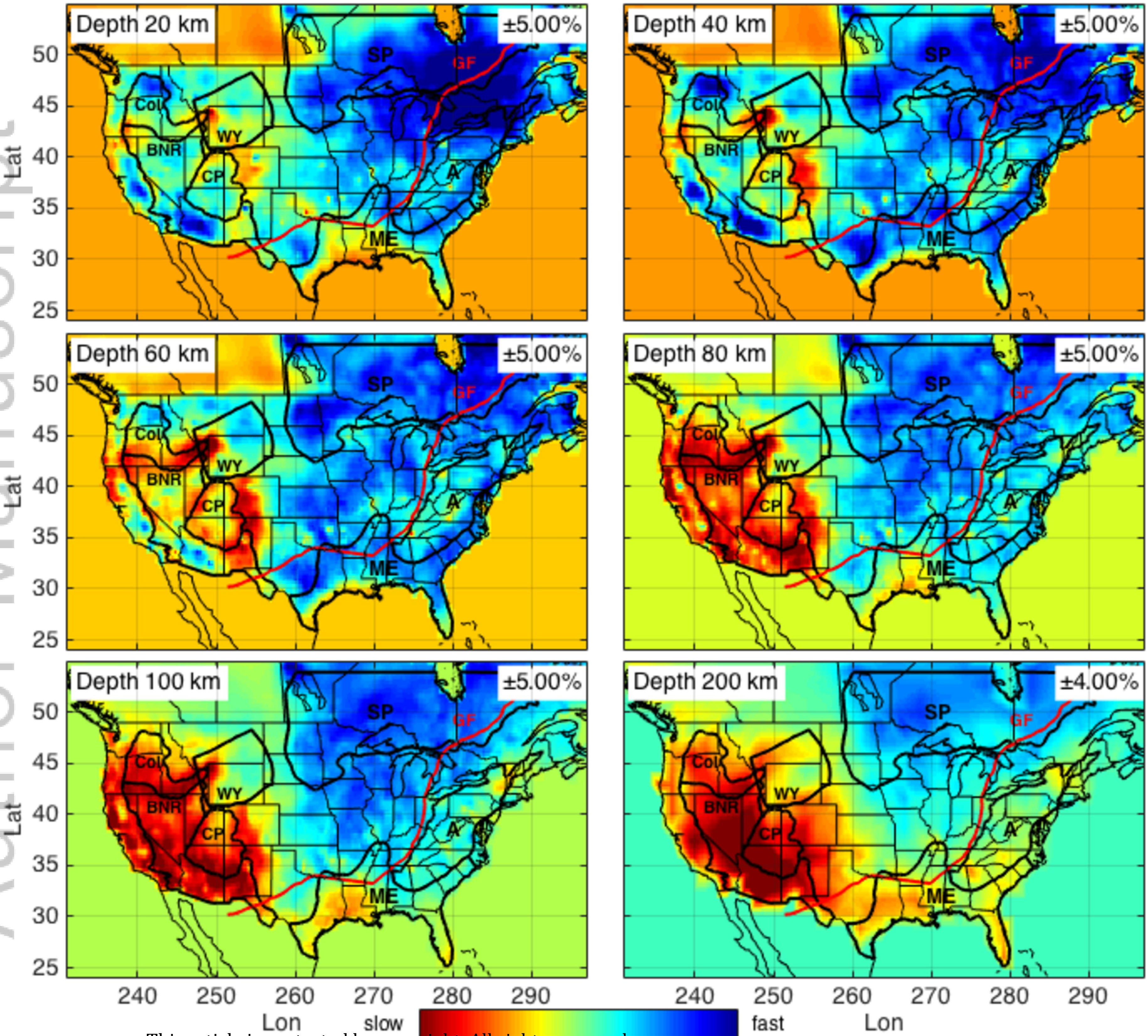
Depth 20 km
±5.00%
Depth 40 km
±5.00%
Depth 60 km
±5.00%
Depth 80 km
±5.00%
Depth 100 km
±5.00%
Depth 200 km
±4.00%
SP
GF
Col
WY
BNR
CP
A
ME
Lat
Lon
slow
fast

Figure 8.

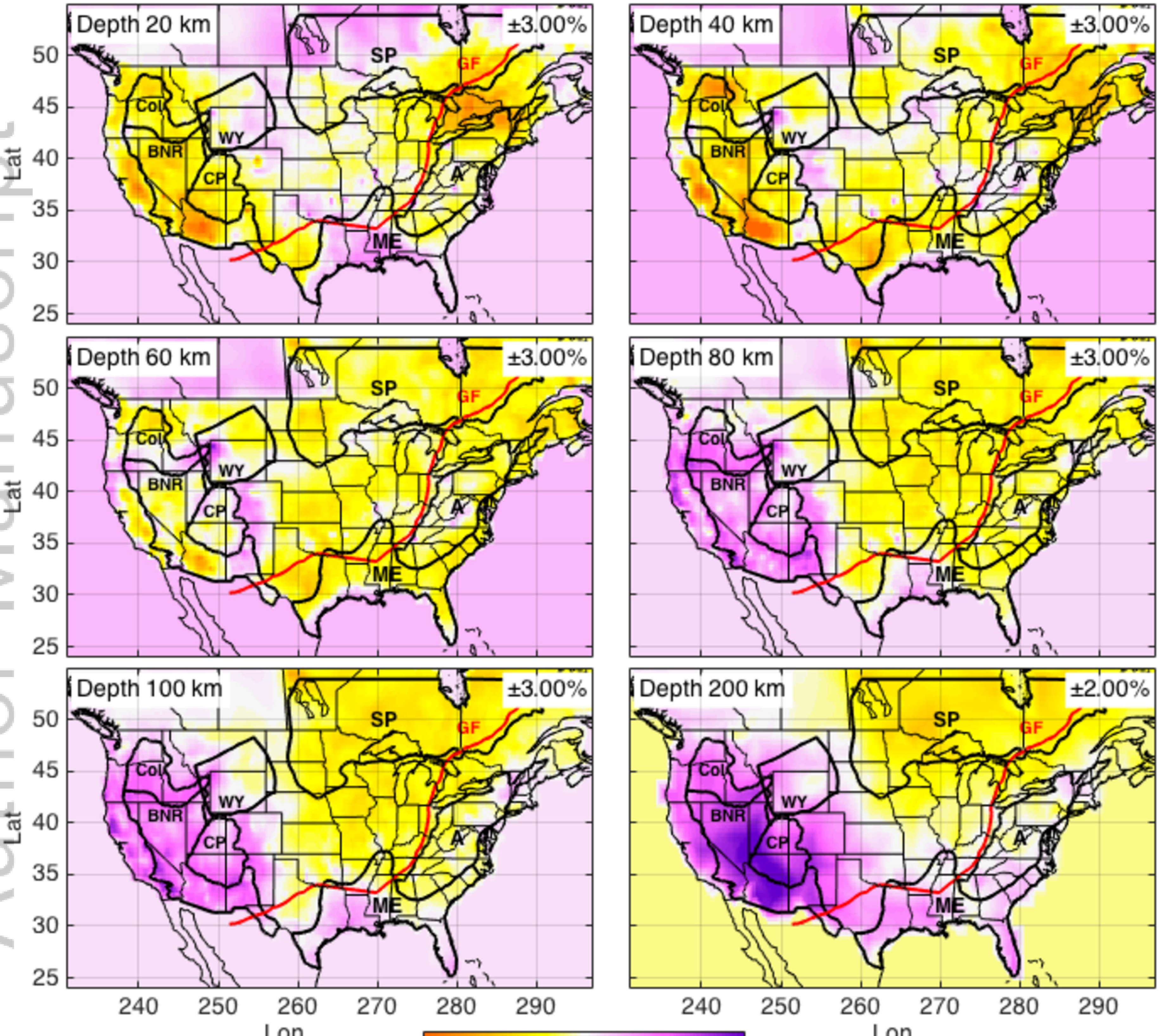

Depth 20 km
±3.00%
Depth 40 km
±3.00%
Depth 60 km
±3.00%
Depth 80 km
±3.00%
Depth 100 km
±3.00%
Depth 200 km
±2.00%
SP
GF
Col
WY
BNR
CP
A
ME
Lat
25
30
35
40
45
50
Lon
240
250
260
270
280
290
-3.0 %
3.0 %

Figure 9.

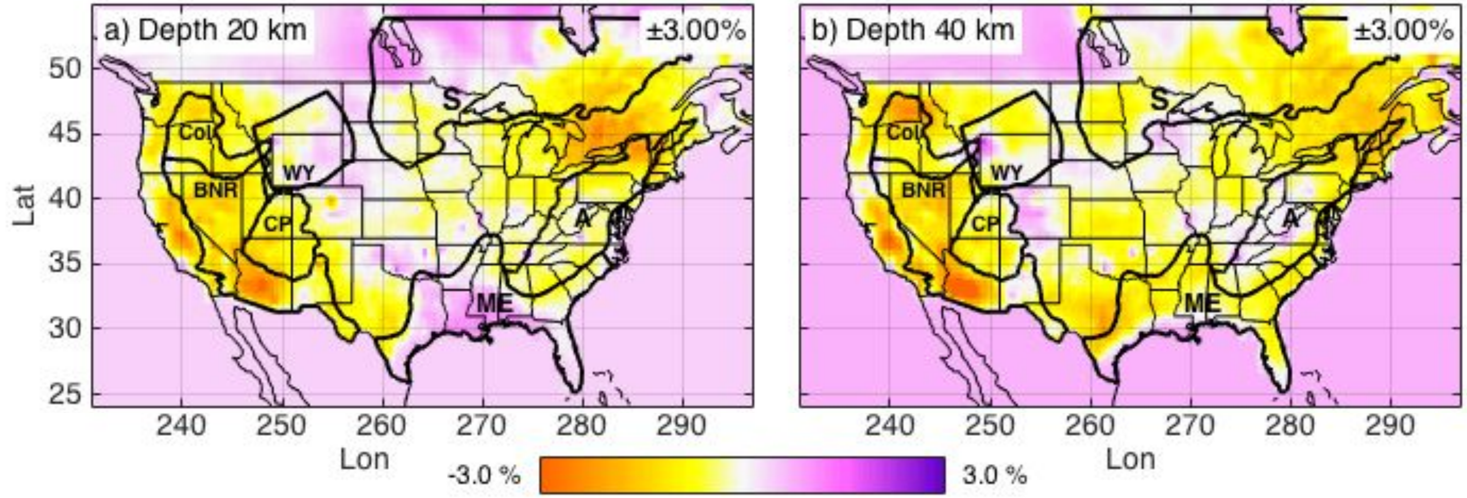

δ(Vp/Vs) (MITPS_20)

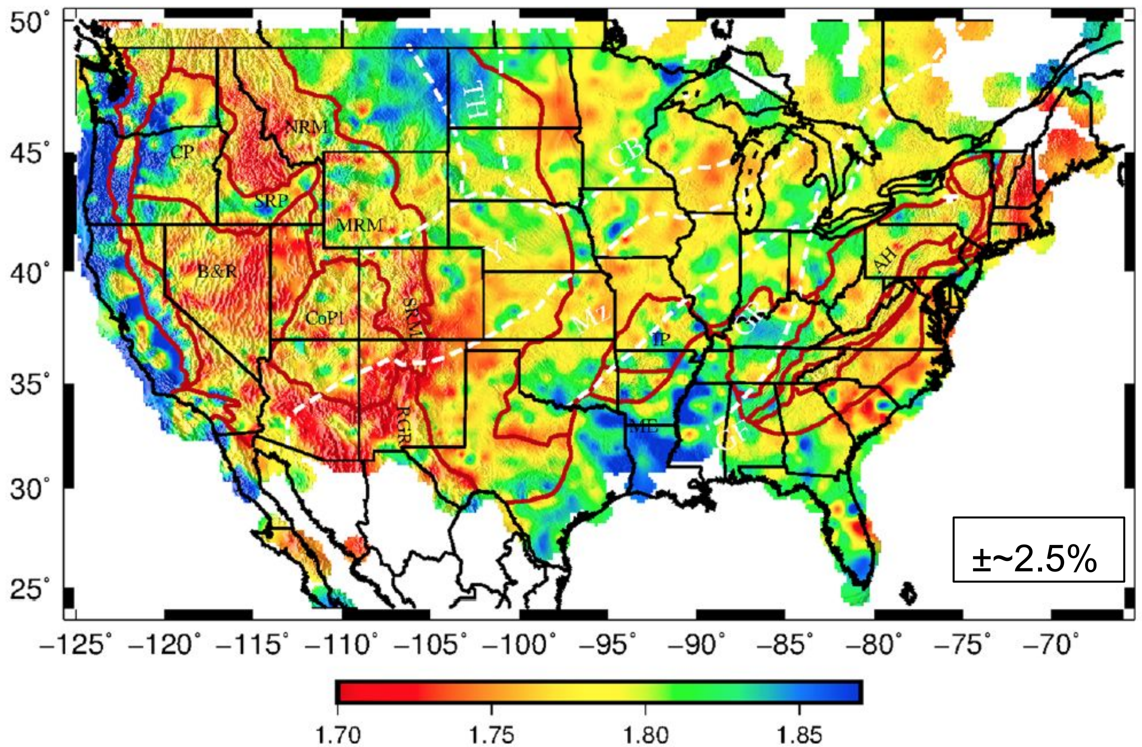

Vp/Vs (Ma & Lowry 2017)

Figure 10.

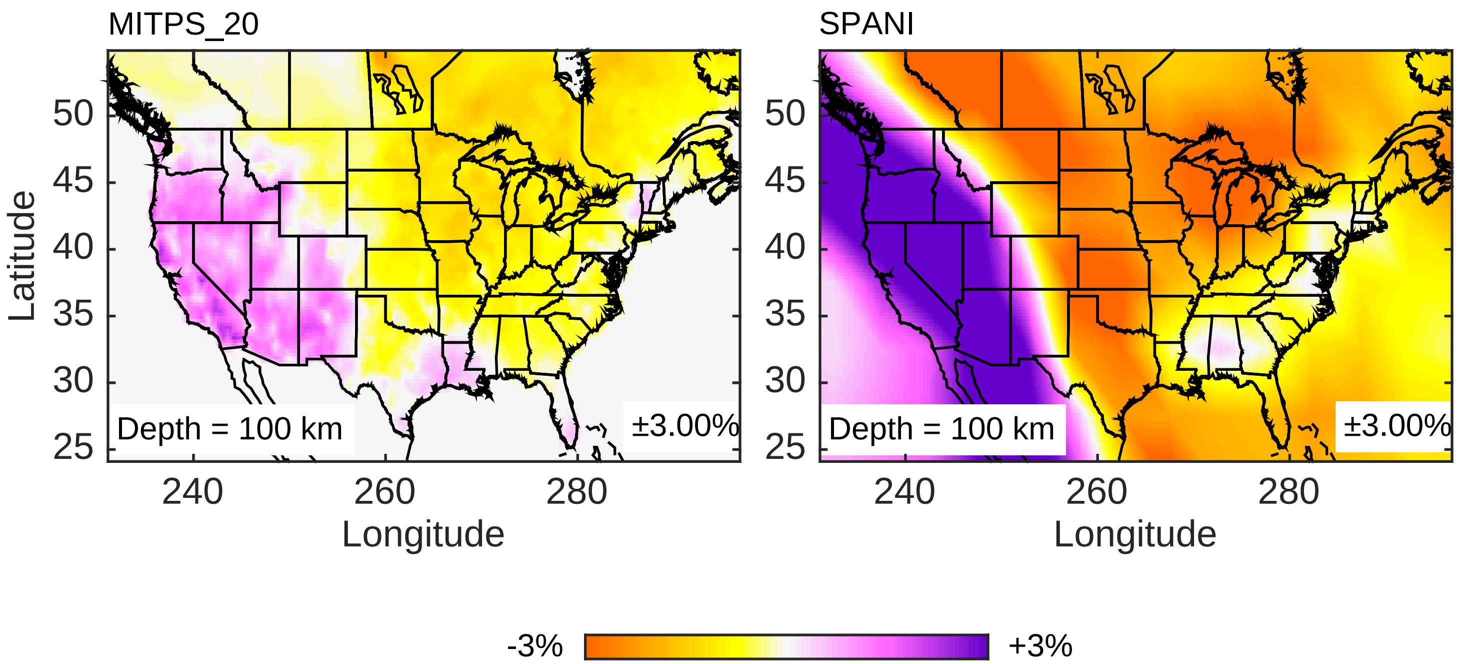
MITPS_20
SPANI
Latitude
50
45
40
35
30
25
Depth = 100 km
±3.00%
240
260
280
Longitude
-3%
+3%

Figure 11.

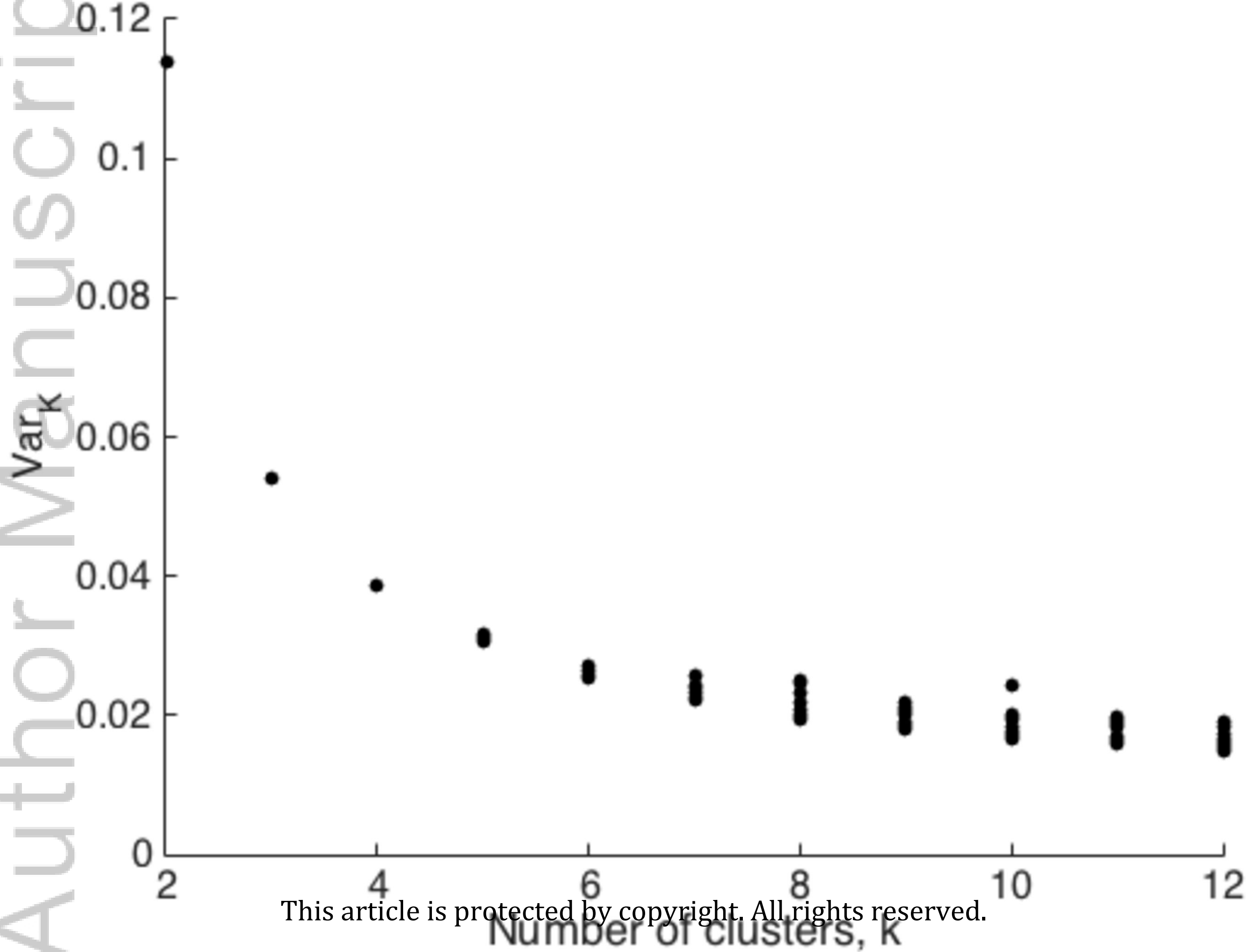

0.12
0.1
0.08
0.06
0.04
0.02
0
Var_k
2
4
6
8
10
12
Number of clusters, k

Figure 12.

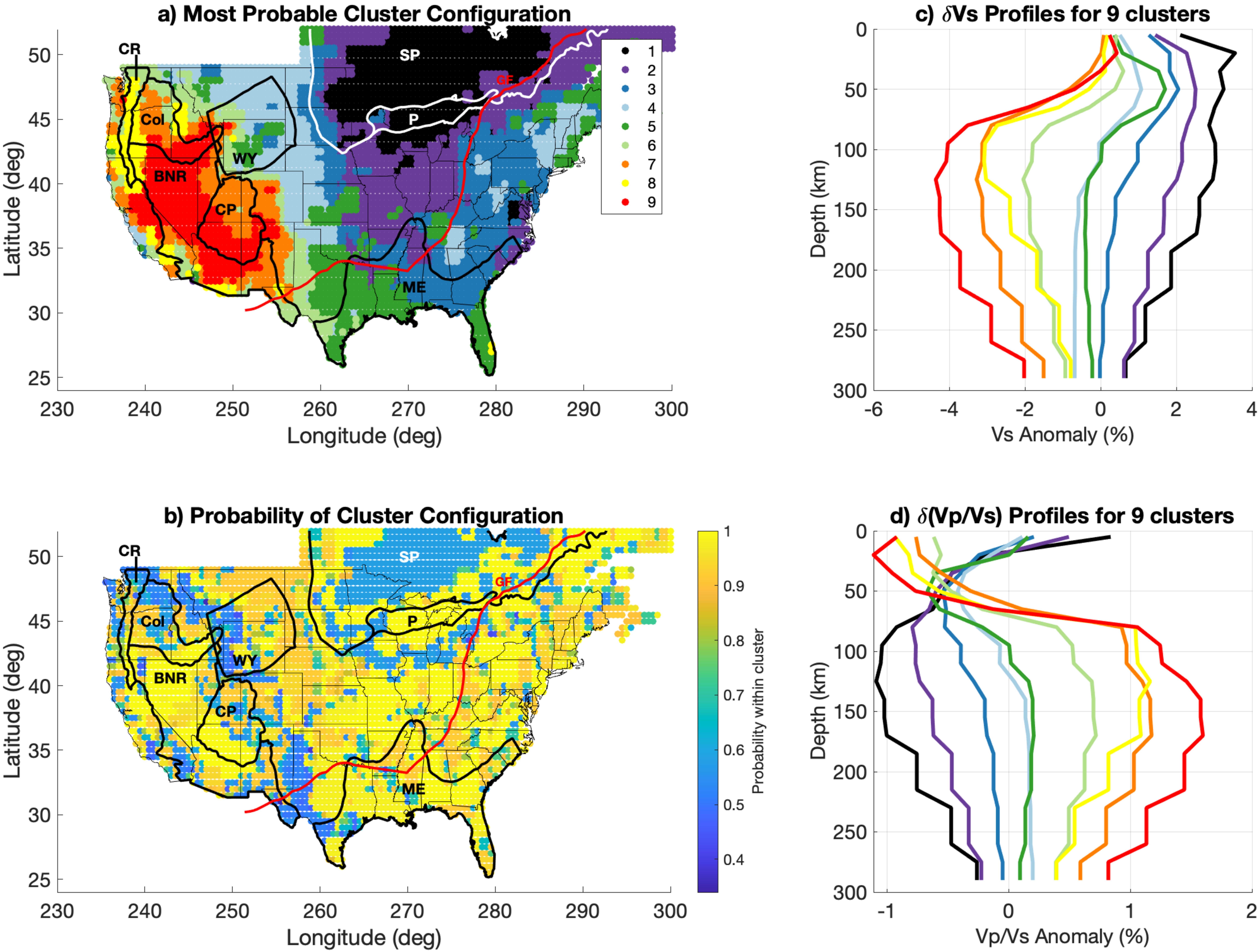

a) Most Probable Cluster Configuration
b) Probability of Cluster Configuration
c) δVs Profiles for 9 clusters
d) δ(Vp/Vs) Profiles for 9 clusters
CR
Col
WY
BNR
CP
SP
P
GF
ME
Latitude (deg)
Longitude (deg)
Depth (km)
Vs Anomaly (%)
Vp/Vs Anomaly (%)
Probability within cluster
1
2
3
4
5
6
7
8
9

Figure 13.

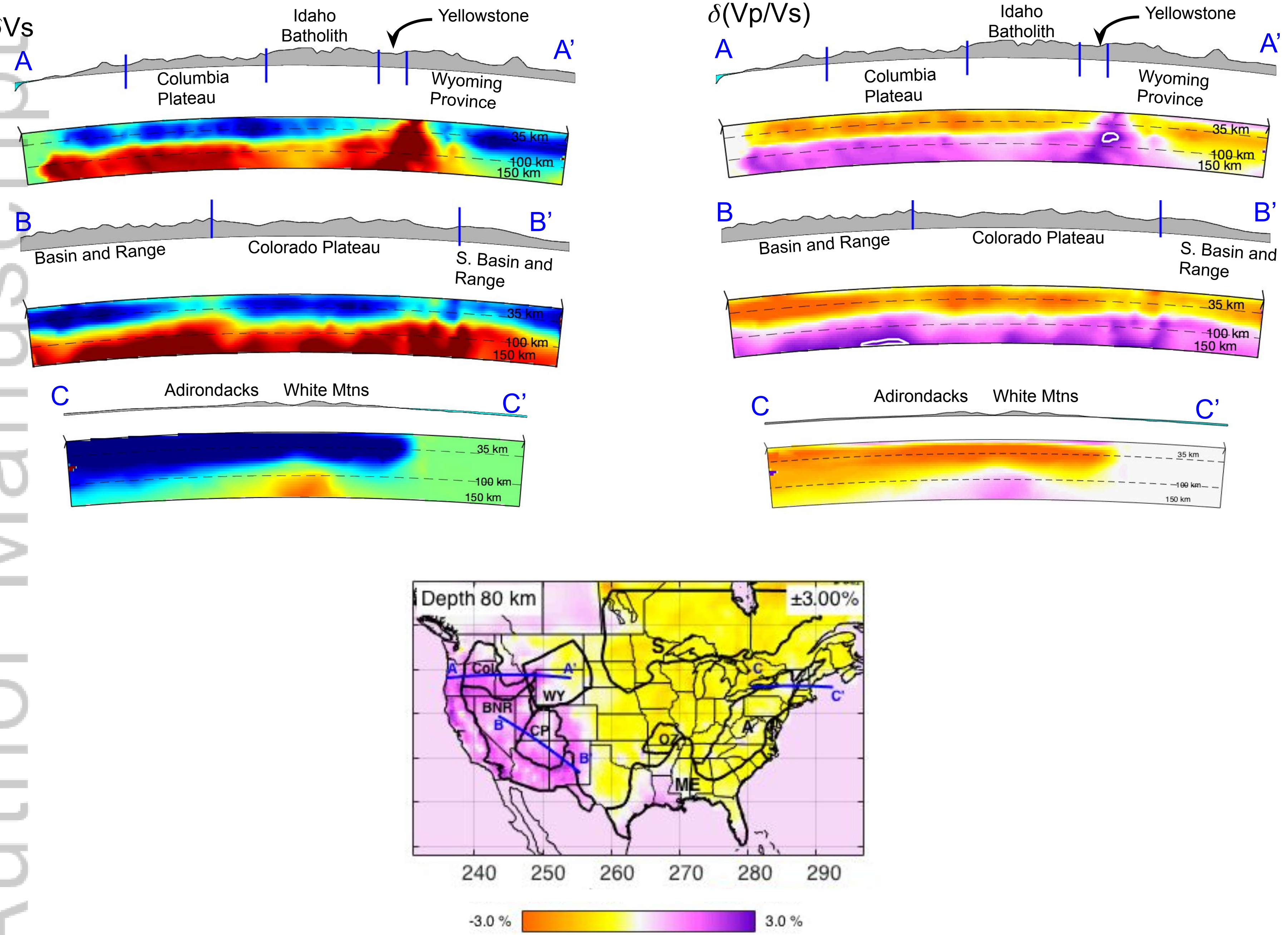
δVs
Idaho Batholith
Yellowstone
A
A'
Columbia Plateau
Wyoming Province
35 km
100 km
150 km
B
B'
Basin and Range
Colorado Plateau
S. Basin and Range
C
C'
Adirondacks
White Mtns
δ(Vp/Vs)
Depth 80 km
±3.00%
Col
WY
BNR
CP
OZ
ME
A
S
240
250
260
270
280
290
-3.0 %
3.0 %

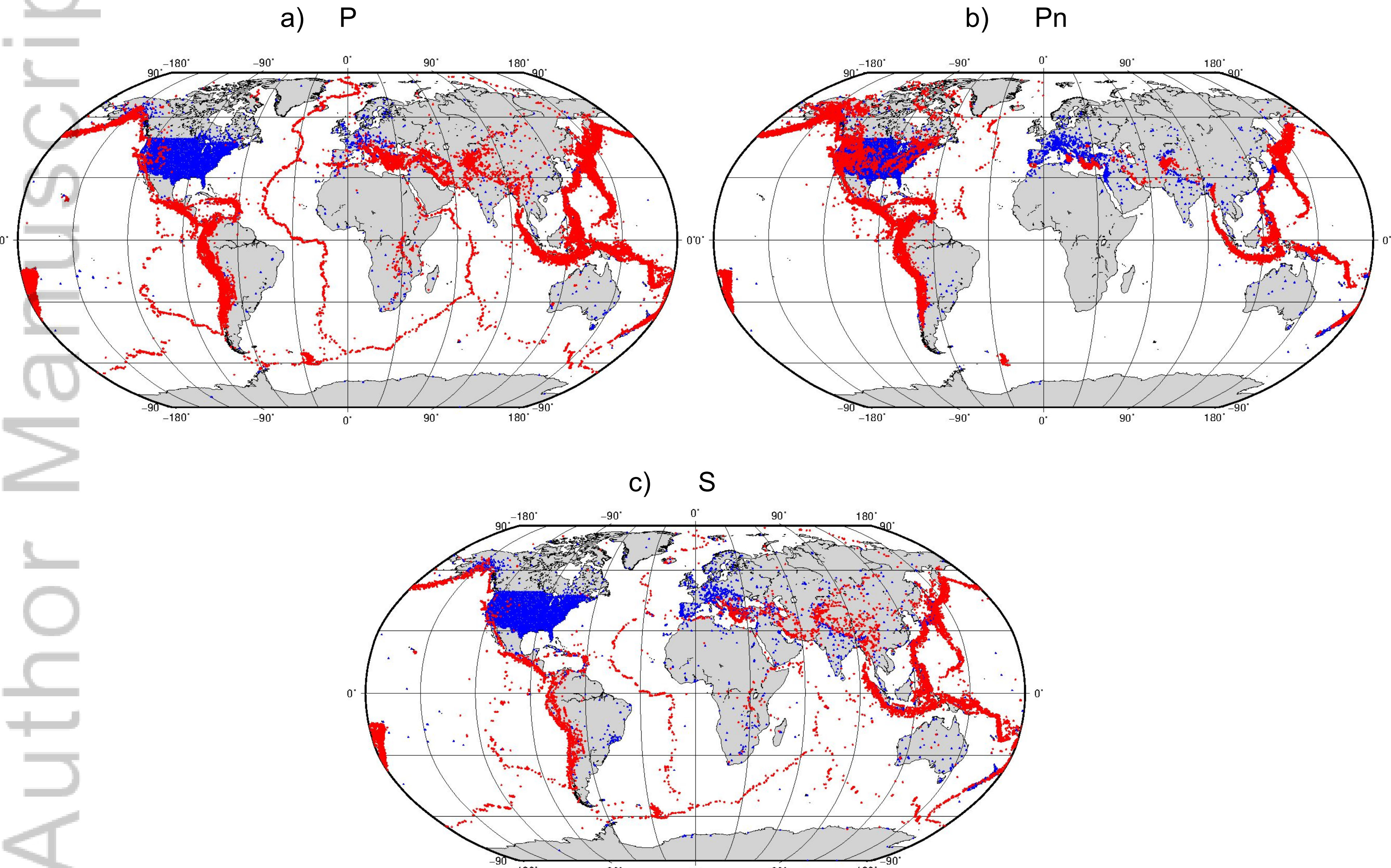
a) P
b) Pn
c) S
−180°
−90°
0°
90°
180°
90°
−90°

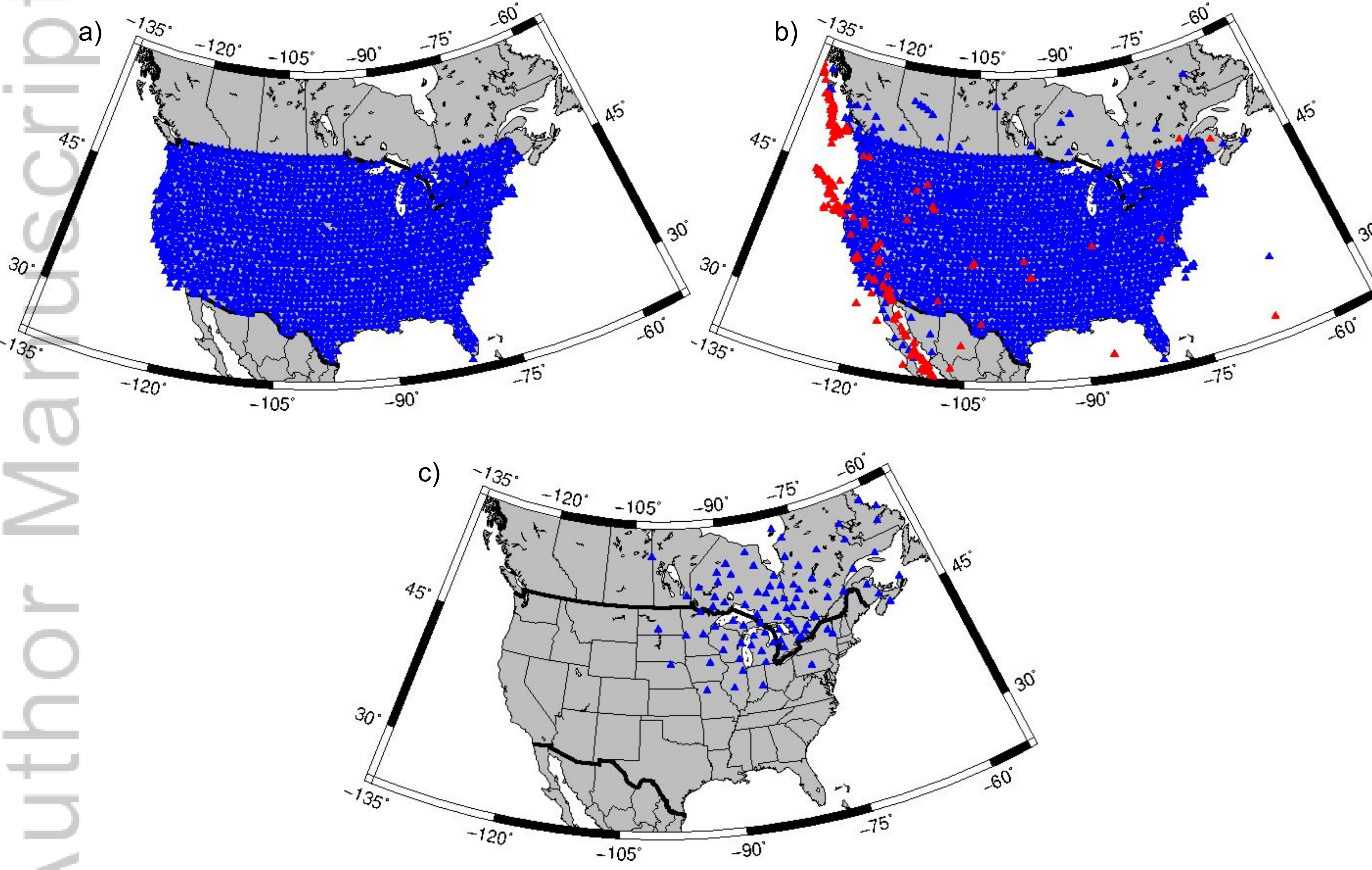
a)
b)
c)
-135°
-120°
-105°
-90°
-75°
-60°
45°
30°

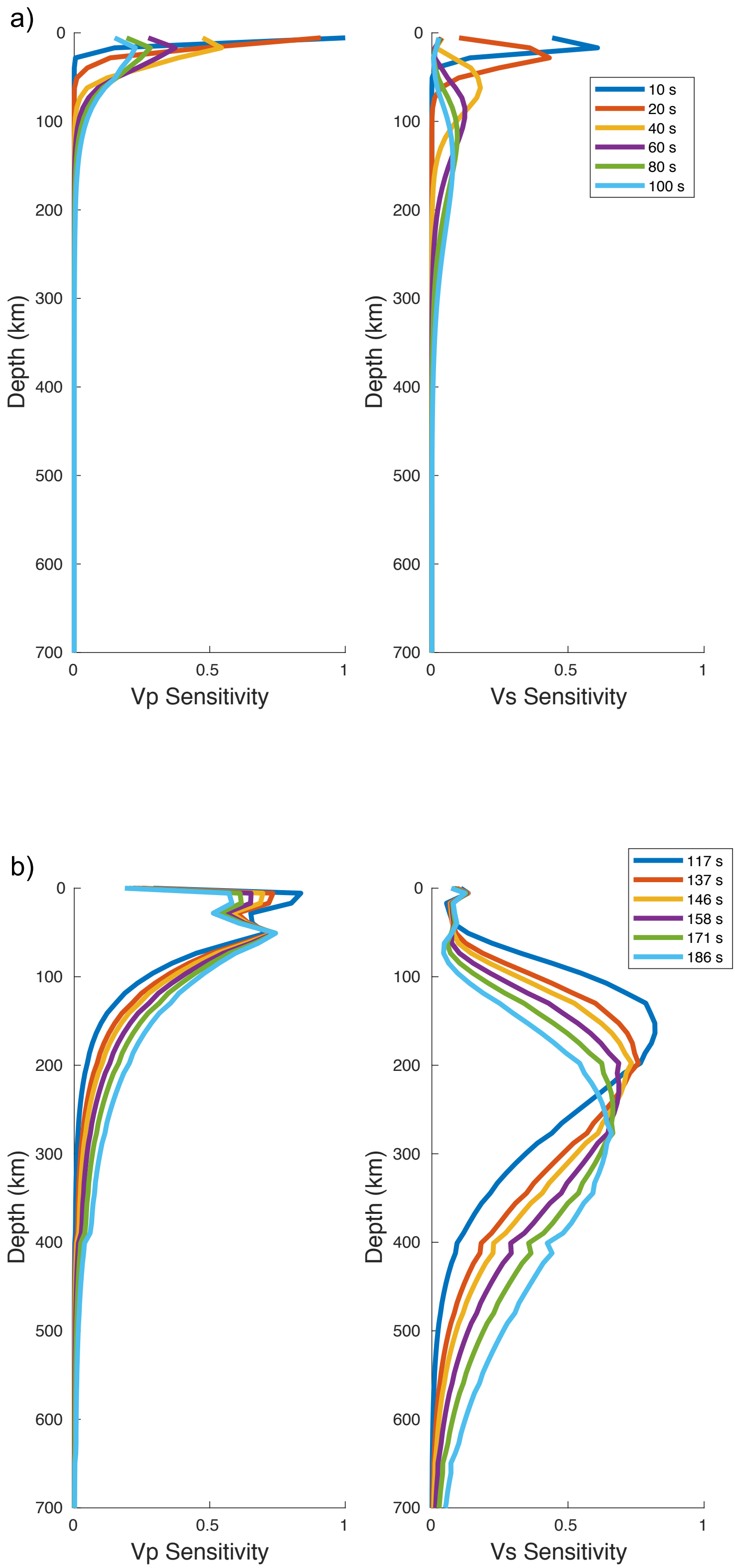
a)
b)
Depth (km)
Vp Sensitivity
Vs Sensitivity
0
100
200
300
400
500
600
700
0
0.5
1
10 s
20 s
40 s
60 s
80 s
100 s
117 s
137 s
146 s
158 s
171 s
186 s

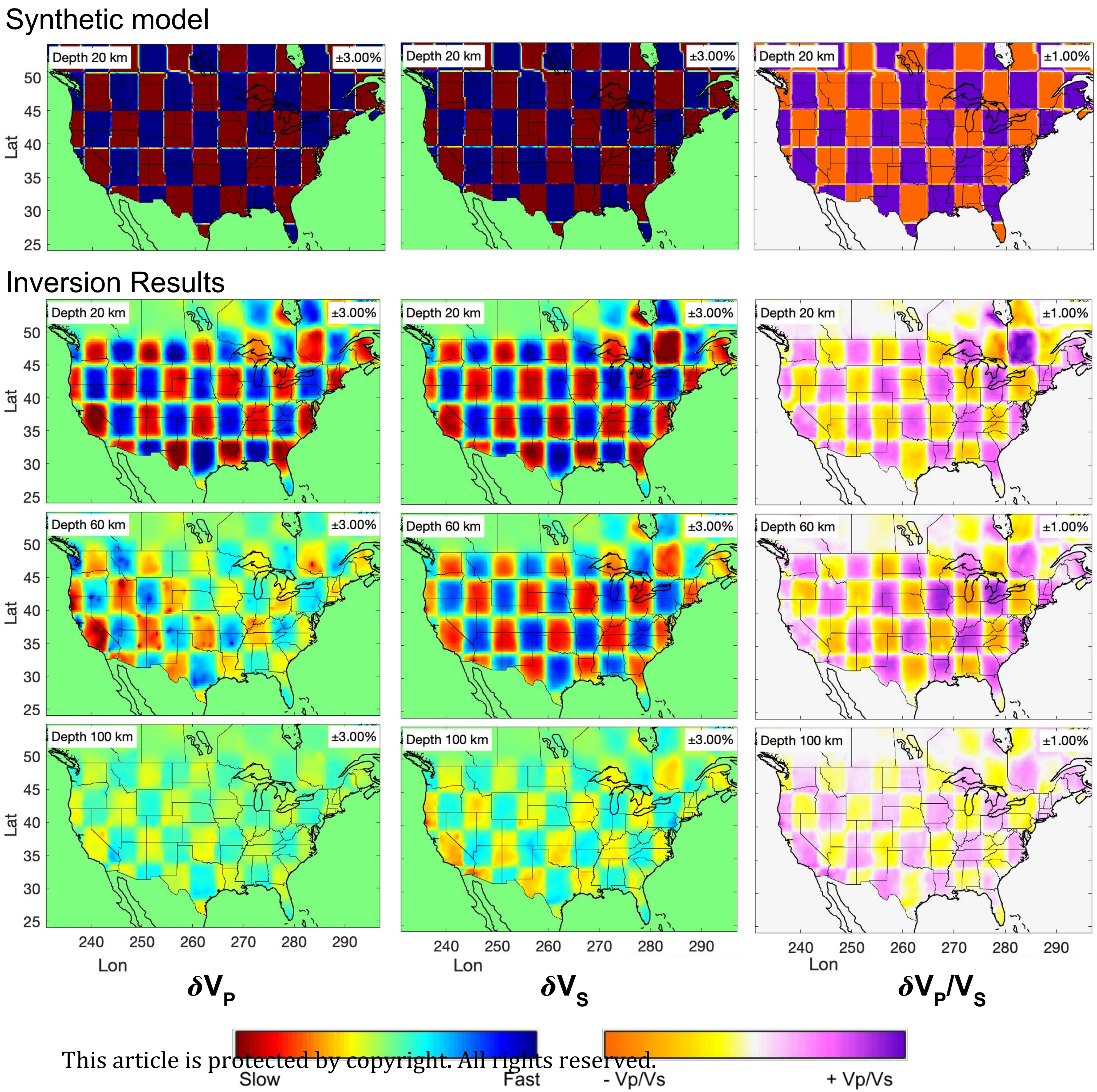
Synthetic model
Inversion Results
Depth 20 km
Depth 60 km
Depth 100 km
±3.00%
±1.00%
Lat
Lon
δVP
δVS
δVP/VS
Slow
Fast
- Vp/Vs
+ Vp/Vs

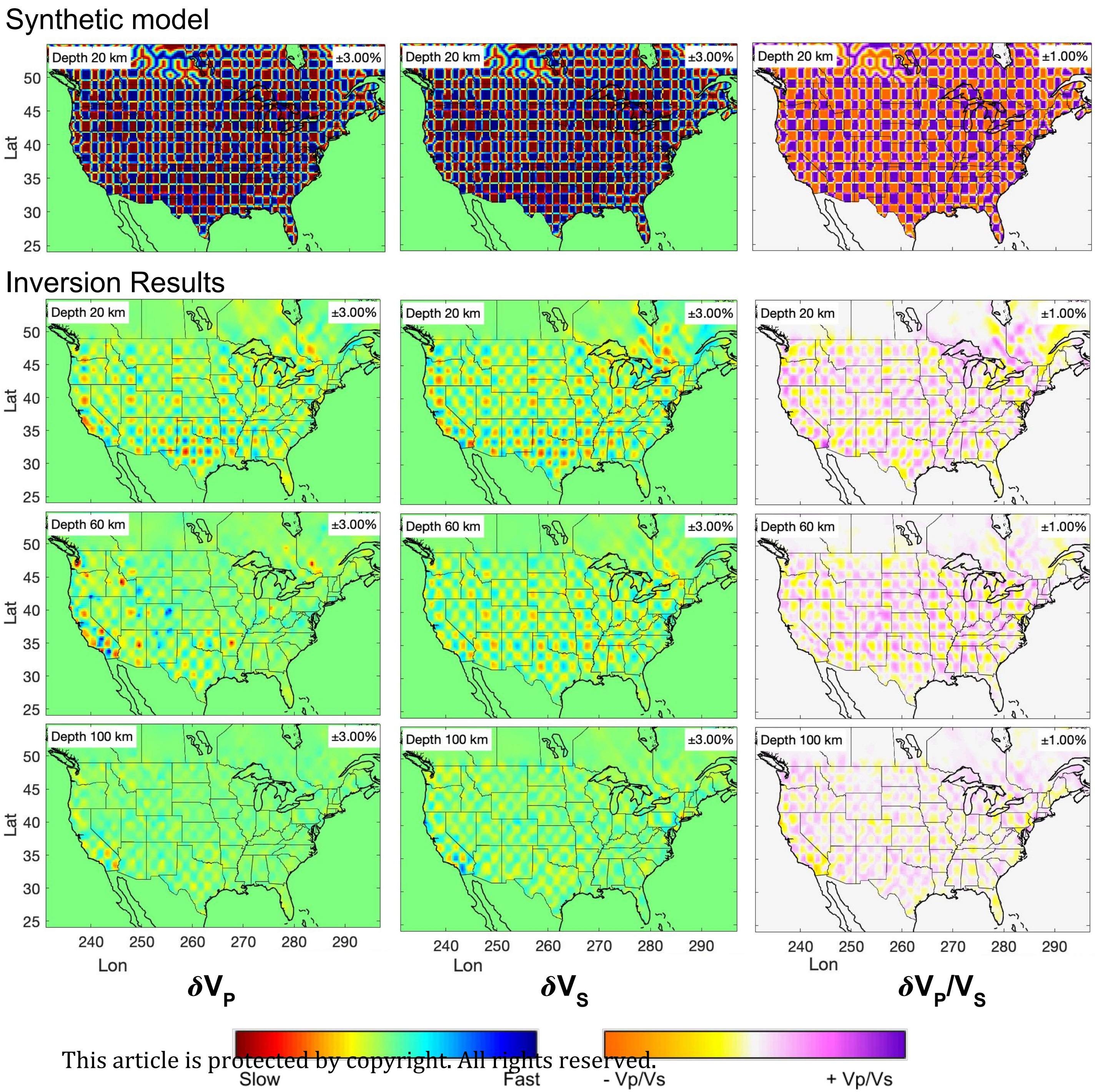

Synthetic model
Inversion Results
Depth 20 km
Depth 60 km
Depth 100 km
±3.00%
±1.00%
Lat
Lon
50
45
40
35
30
25
240
250
260
270
280
290
δV_P
δV_S
δV_P/V_S
Slow
Fast
- Vp/Vs
+ Vp/Vs

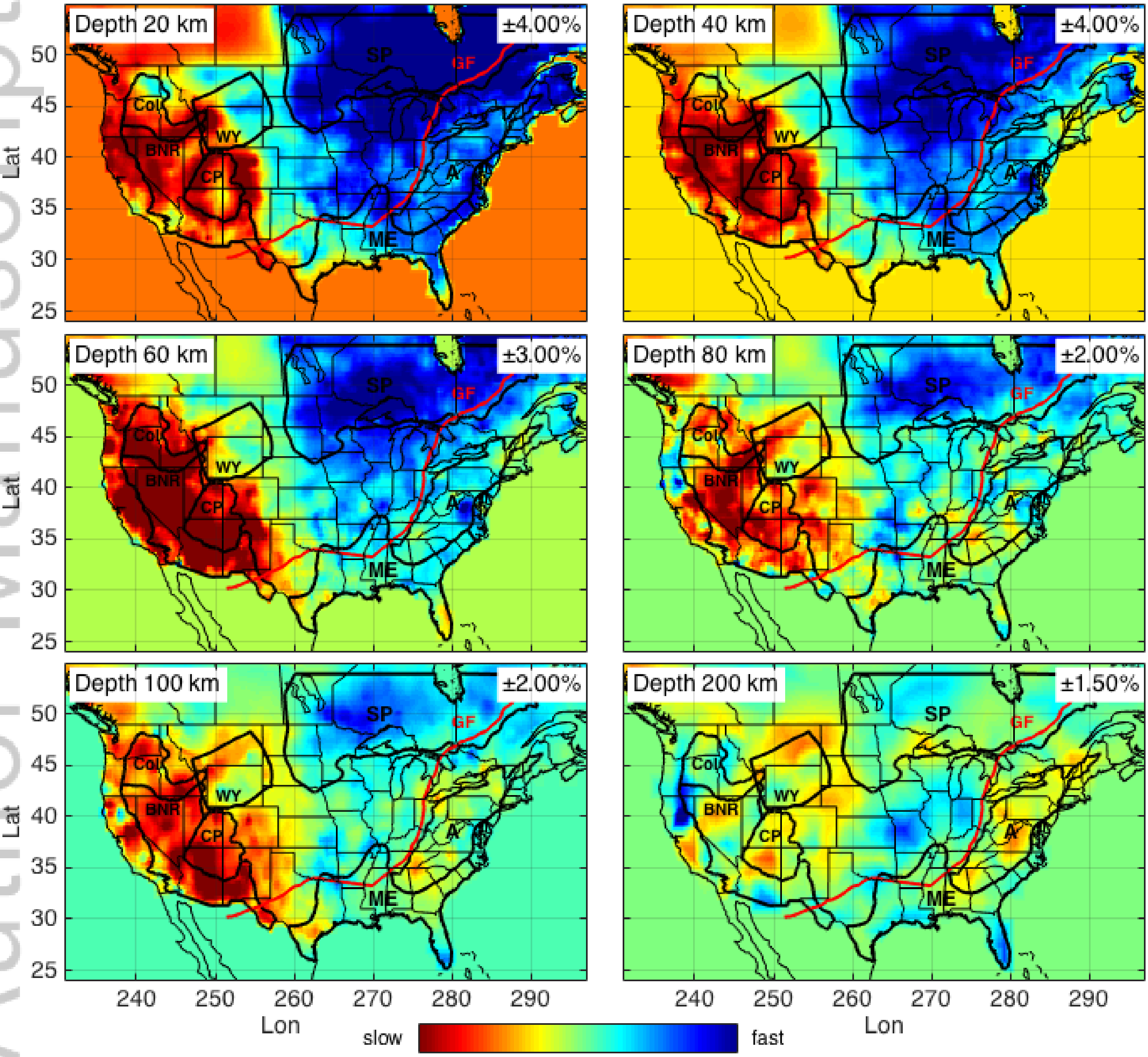

JGRB_54570_2020JB020574-f06-z-.png

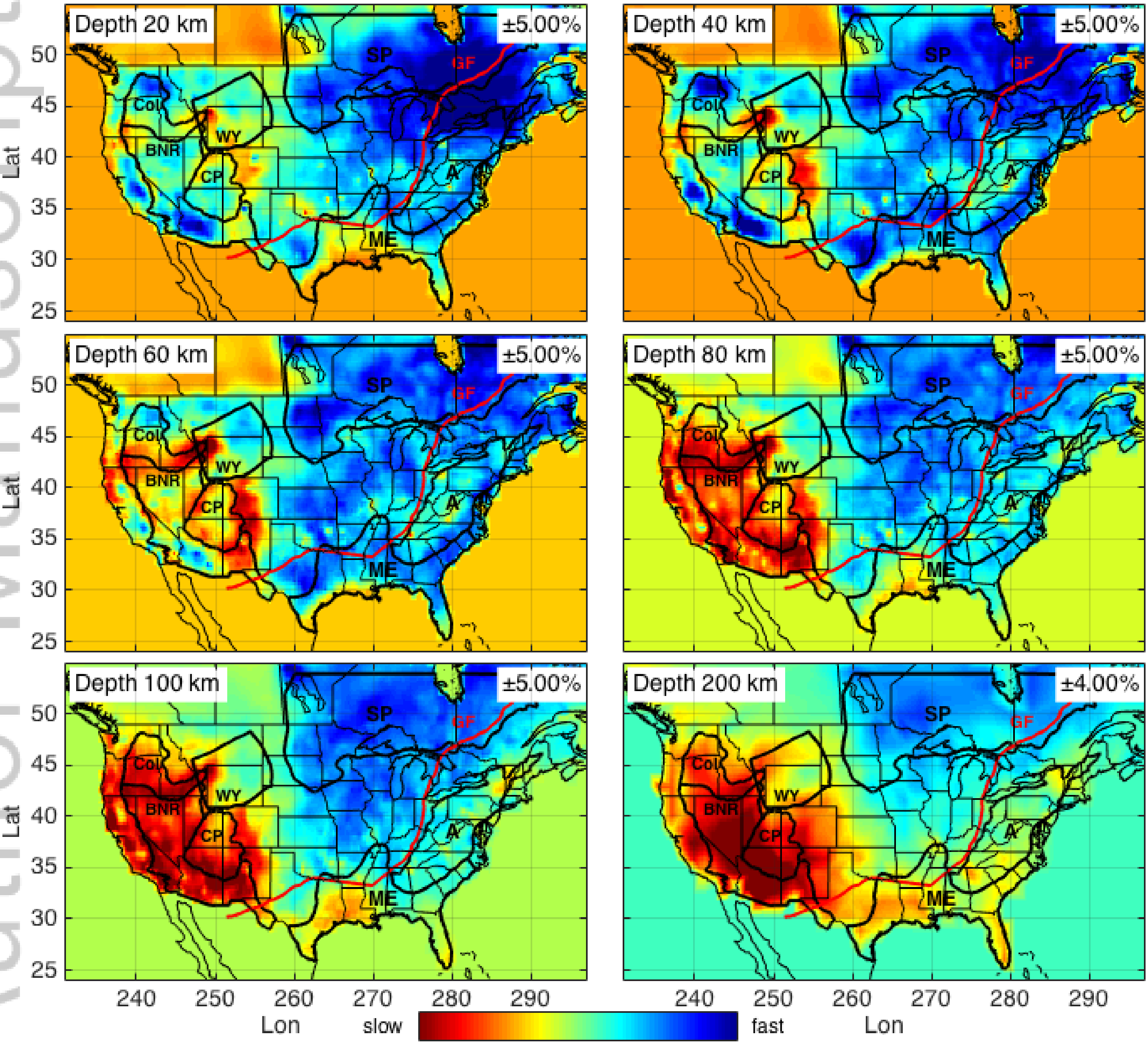

JGRB_54570_2020JB020574-f07-z-.png

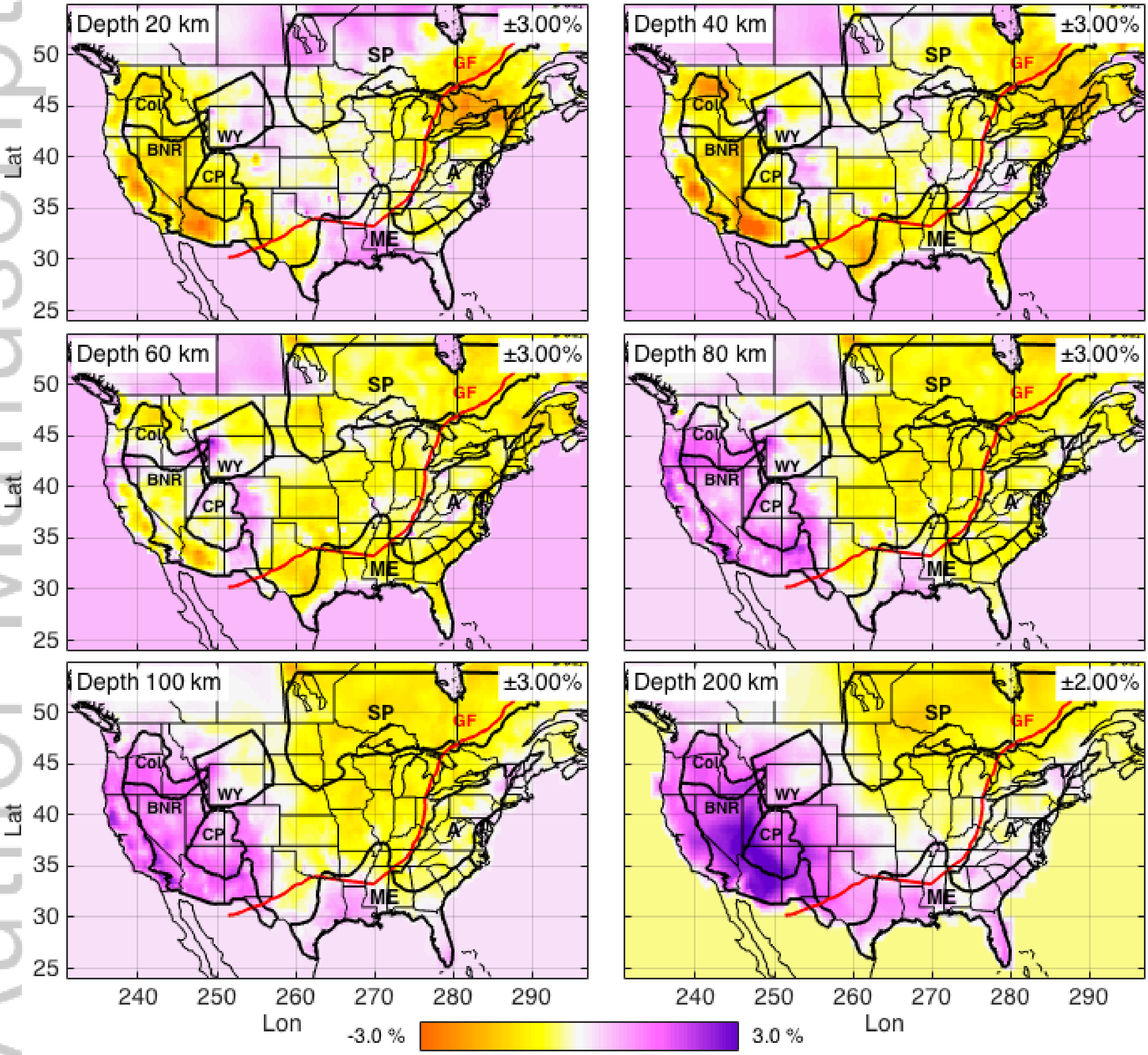

JGRB_54570_2020JB020574-f08-z-.png

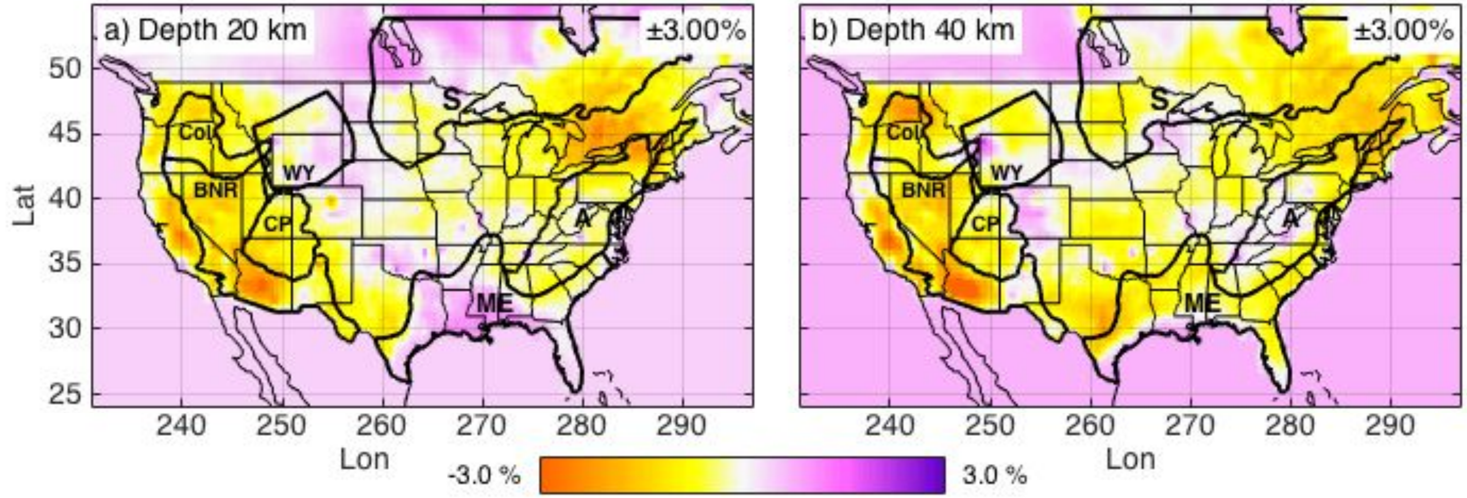

δ(Vp/Vs) (MITPS_20)

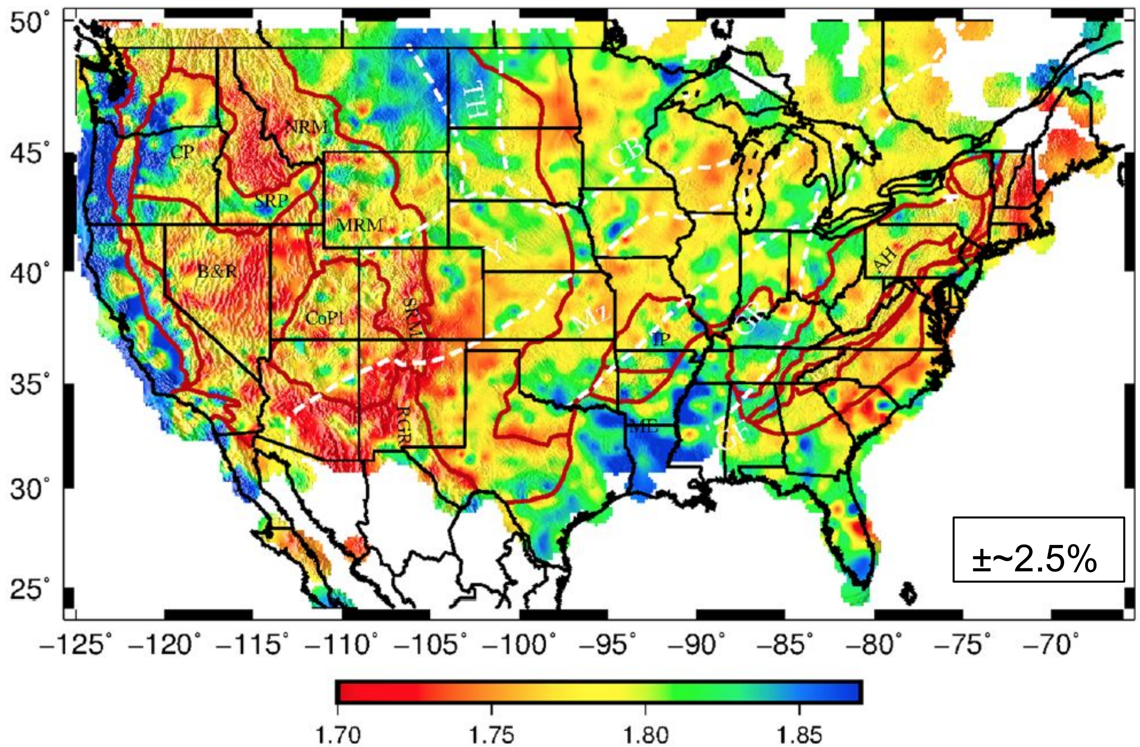

Vp/Vs (Ma & Lowry 2017)

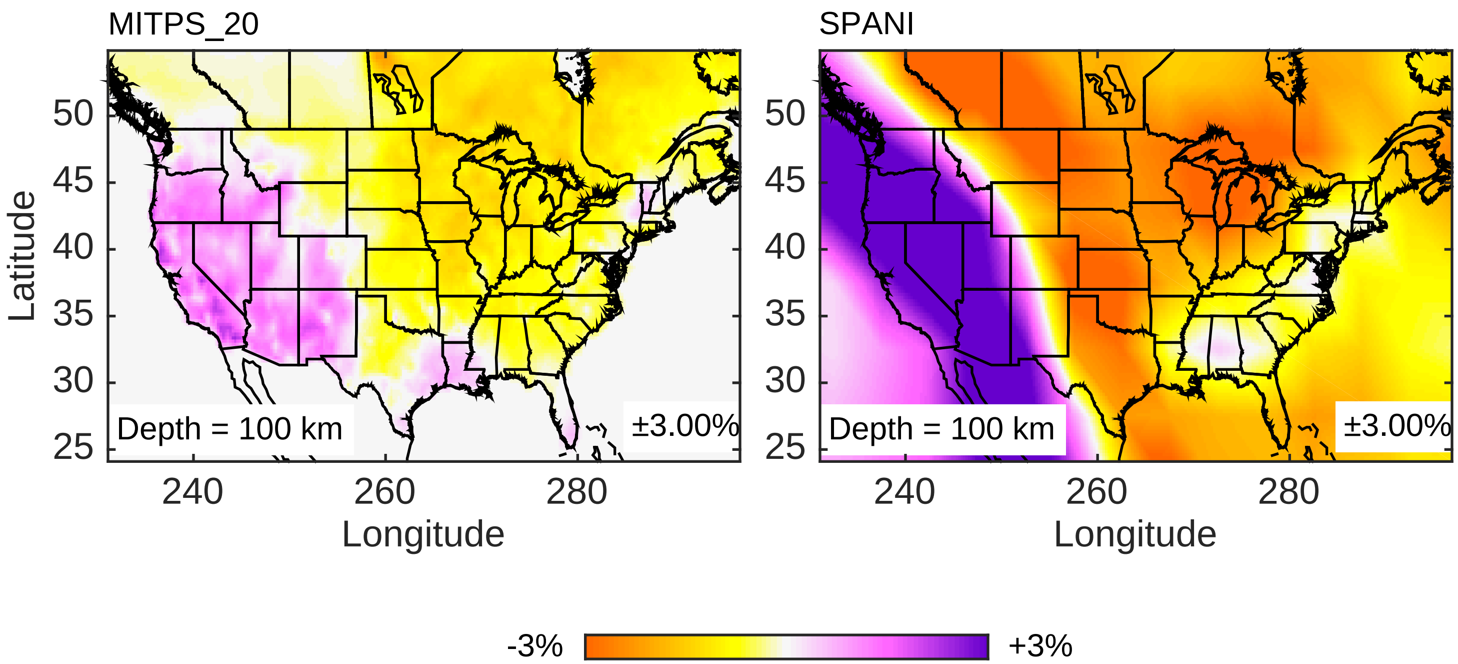
MITPS_20
SPANI
Latitude
50
45
40
35
30
25
240
260
280
Longitude
Depth = 100 km
±3.00%
-3%
+3%

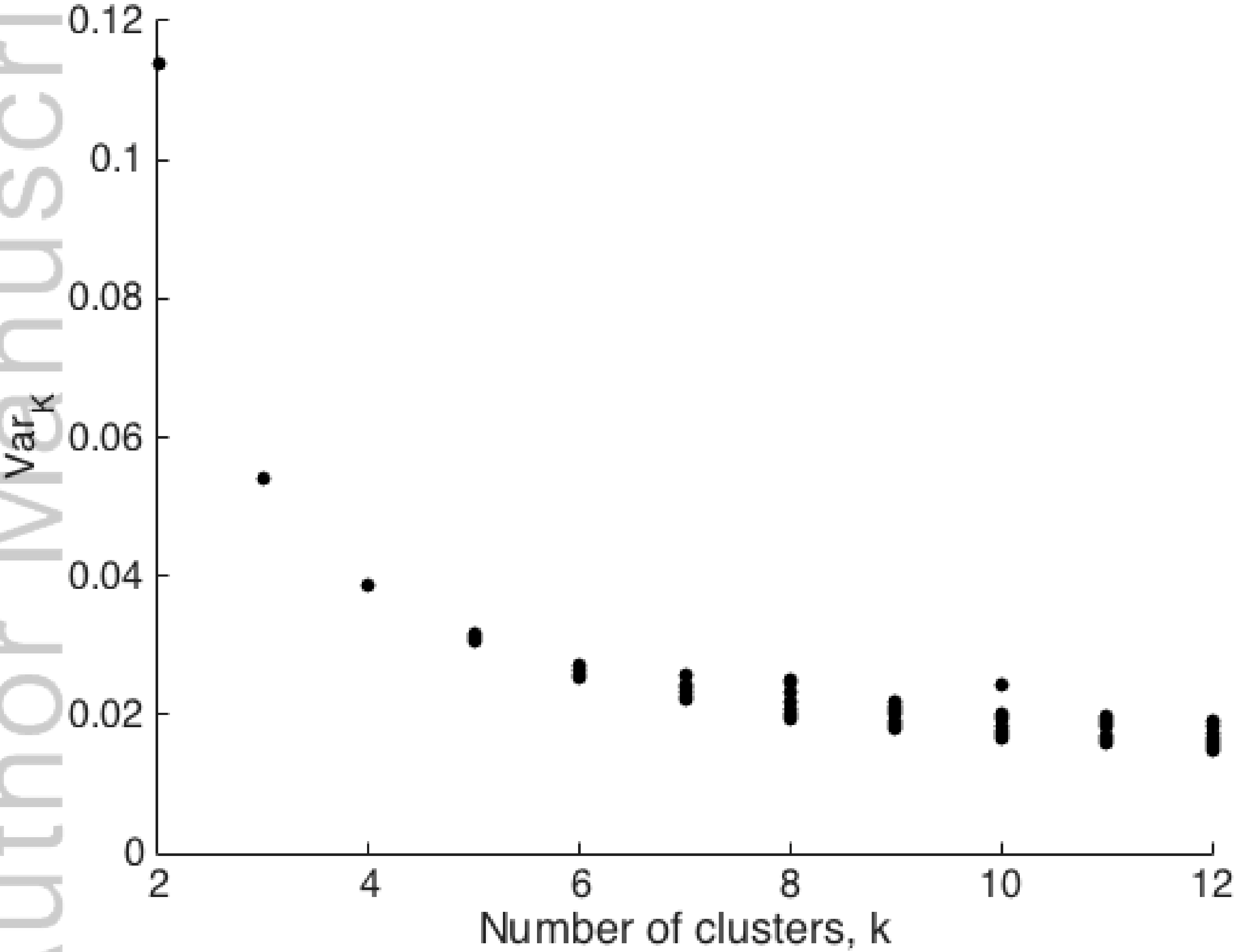

JGRB_54570_2020JB020574-f11-z-.png

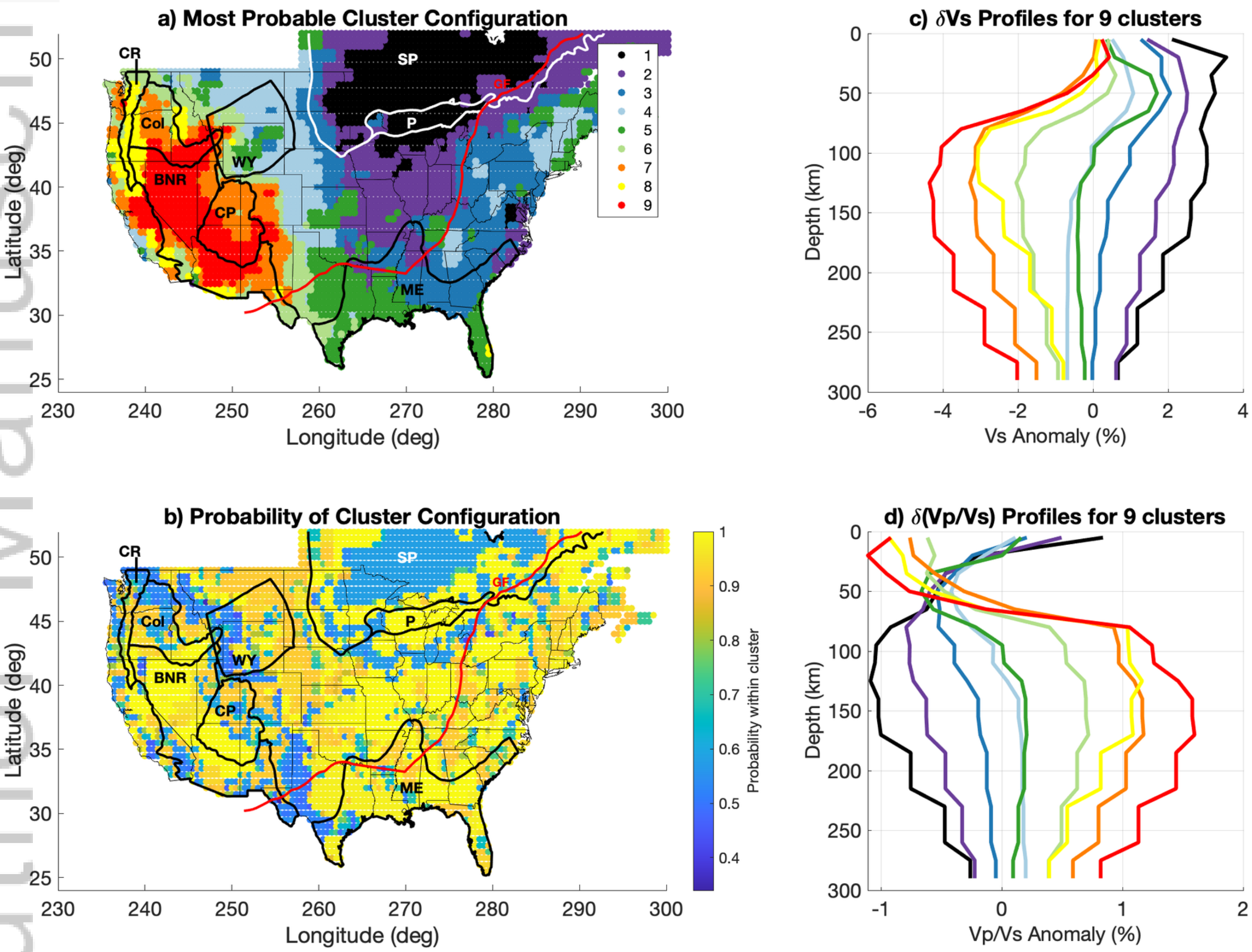

JGRB_54570_2020JB020574-f12-z-.png

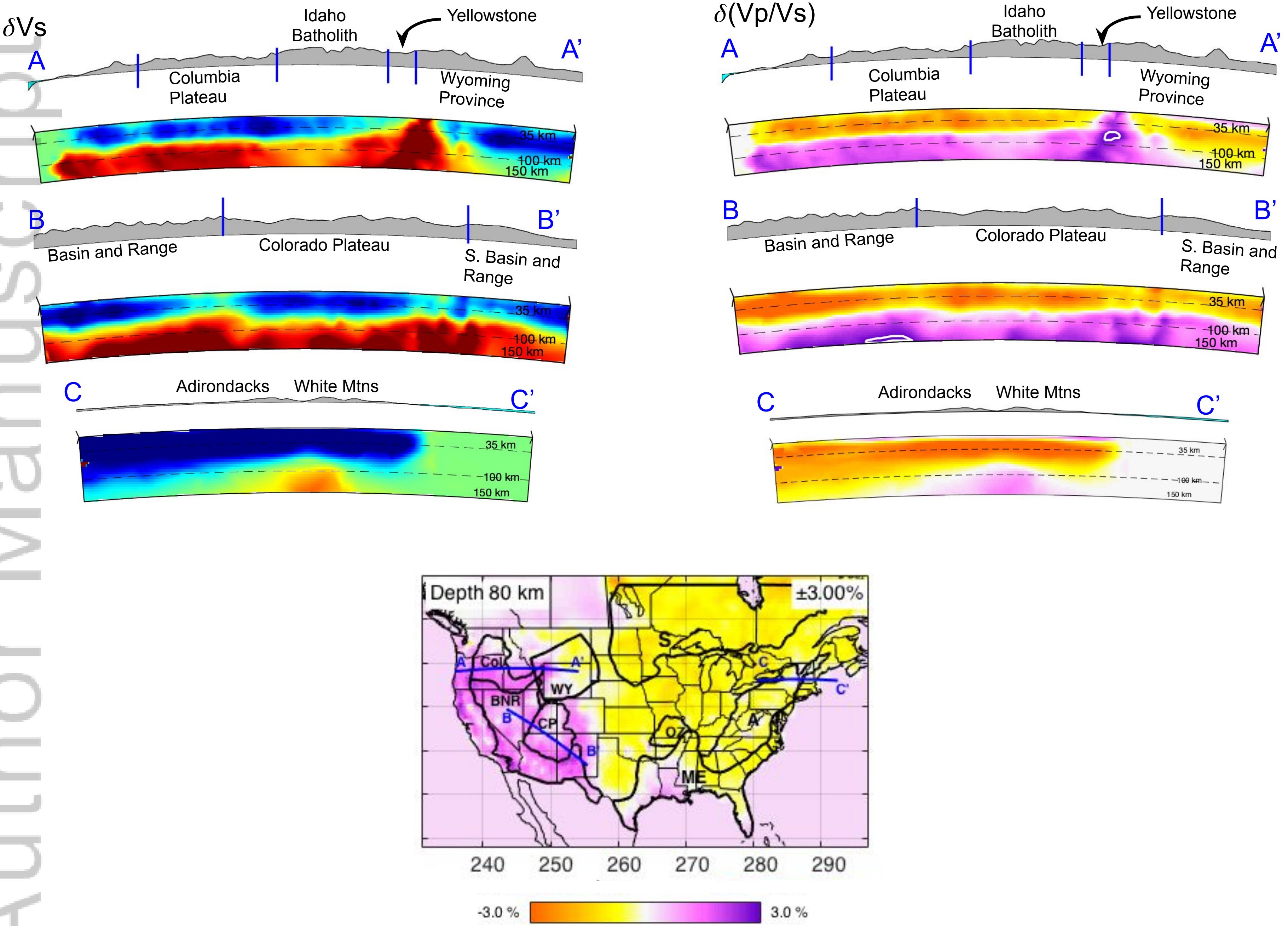

δVs
A
Idaho Batholith
Yellowstone
A'
Columbia Plateau
Wyoming Province
35 km
100 km
150 km
B
B'
Basin and Range
Colorado Plateau
S. Basin and Range
35 km
100 km
150 km
C
Adirondacks
White Mtns
C'
35 km
100 km
150 km
δ(Vp/Vs)
A
Idaho Batholith
Yellowstone
A'
Columbia Plateau
Wyoming Province
35 km
100 km
150 km
B
B'
Basin and Range
Colorado Plateau
S. Basin and Range
35 km
100 km
150 km
C
Adirondacks
White Mtns
C'
Depth 80 km
±3.00%
Col
WY
BNR
CP
S
OZ
ME
240
250
260
270
280
290
-3.0 %
3.0 %